UNIVERSIDADE ESTADUAL DE CAMPINAS
Faculdade de Engenharia Elétrica e de Computação

Livia Maria de Aguiar Rodrigues

Common Carotid Artery Lumen Automatic Segmentation from Cine Fast Spin Echo Magnetic Resonance Imaging

Segmentação Automática do Lúmen da Carótida Comum Utilizando Imagens de Ressonância Magnética Cine Fast Spin Echo

Campinas

2018

Livia Maria de Aguiar Rodrigues

Common Carotid Artery Lumen Automatic Segmentation from Cine Fast Spin Echo Magnetic Resonance Imaging

Segmentação Automática do Lúmen da Carótida Comum Utilizando Imagens de Ressonância Magnética Cine Fast Spin Echo

Dissertation presented to the School of Electrical and Computer Engineering of the University of Campinas in partial fulfillment of the requirements for the degree of Master in Electrical Engineering, in the area of Computer Engineering.
Dissertação apresentada à Faculdade de Engenharia Elétrica e de Computação da Universidade Estadual de Campinas como parte dos requisitos exigidos para a obtenção do título de Mestra em Engenharia Elétrica, na Àrea de Engenharia da Computação

Supervisor: Prof. Dr. Roberto de Alencar Lotufo

Este exemplar corresponde à versão final da tese defendida pelo aluno Livia Maria de Aguiar Rodrigues, e orientada pelo Prof. Dr. Roberto de Alencar Lotufo

Campinas

2018

Agência(s) de fomento e nº(s) de processo(s): CAPES

Ficha catalográfica
Universidade Estadual de Campinas
Biblioteca da Área de Engenharia e Arquitetura
Rose Meire da Silva - CRB 8/5974

Rodrigues, Livia Maria de Aguiar, 1990-
R618c Common carotid artery lumen automatic segmentation from cine fast spin echo magnetic resonance imaging / Livia Maria de Aguiar Rodrigues. – Campinas, SP : [s.n.], 2018.

Orientador: Roberto de Alencar Lotufo.
Dissertação (mestrado) – Universidade Estadual de Campinas, Faculdade de Engenharia Elétrica e de Computação.

1. Segmentação de imagens médicas. 2. Imagem de ressonância magnética. 3. Artéria carótida. I. Lotufo, Roberto de Alencar, 1955-. II. Universidade Estadual de Campinas. Faculdade de Engenharia Elétrica e de Computação. III. Título.

Informações para Biblioteca Digital

Título em outro idioma: Segmentação automática do lúmen da catótida comum utilizando imagens de ressonância magnética cine fast spin echo
Palavras-chave em inglês:
Segmentation of medical images
Magnetic resonance imaging
Carotid artery
Área de concentração: Engenharia de Computação
Titulação: Mestra em Engenharia Elétrica
Banca examinadora:
Roberto de Alencar Lotufo [Orientador]
Richard Frayne
Léo Pini Magalhães
Data de defesa: 16-10-2018
Programa de Pós-Graduação: Engenharia Elétrica

COMISSÃO JULGADORA - DISSERTAÇÃO DE MESTRADO

Candidata: Livia Maria de Aguiar Rodrigues RA: 180545
Data da Defesa: 16 de outubro de 2018
Título da Tese: Common Carotid Artery Lumen Automatic Segmentation from Cine Fast Spin Echo Magnetic Resonance Imaging

Prof. Dr. Roberto de Alencar Lotufo (Presidente, FEEC/UNICAMP)
Prof. Dr. Léo Pini Magalhães (FEEC/UNICAMP)
Prof. Dr. Richard Frayne (University of Calgary)

Ata de defesa, com as respectivas assinaturas dos membros da Comissão Julgadora, encontra-se no processo de vida acadêmica do aluno.

Acknowledgements

Agradeço inicialmente a meu orientador, prof. Roberto Lotufo e a professora Letícia Ritner pelos ensinamentos passados durante esses anos. A Roberto Souza, colega de laboratório e querido amigo, agradeço imensamente por todo o auxílio técnico e motivacional durante o projeto. A meus amigos do laboratório, em especial a meus colegas do MicLab, obrigada pelo companherismo do dia a dia. A meus pais, Cecília e Frederico, agradeço por sempre me darem a força que necessitava para seguir adiante. A meus irmãos, por serem sempre um exemplo de comprometimento e profissionalismo. Agradeço a meu marido, Alexandre, por me apoiar de todas as formas e durante todos os dias dessa jornada. Por fim, agradeço a meu filho, Arthur, que todos os dias me faz querer ser uma pessoa melhor. O presente trabalho foi realizado com apoio da Coordenação de Aperfeiçoamento de Pessoal de Nível Superior - Brasil (CAPES) - Código de Financiamento 001.

Abstract

Atherosclerosis is one of the main causes of stroke and is responsible for millions of deaths per year. Magnetic resonance (MR) is a common way of assessing carotid artery atherosclerosis. A newly proposed cine fast spin echo (FSE) MR imaging method can now obtain dynamic MR data (*i.e.*, generate images across the cardiac cycle). This work introduces a post-processing technique that automatically segments the common carotid artery (CCA) wall-blood boundary (lumen) across the cardiac cycle with no need of human interaction. To the best of our knowledge, this work is the first proposed technique for segmenting cardiac cycle-resolved cine FSE images. The technique overcomes some limitations of dynamic compared to static images (*e.g.*, lower spatial resolution). It combines *a priori* knowledge about the size and shape of the CCA, with the max-tree data structure, random forest classifier and tie-zone watershed transform from identified internal and external markers to segment the vessel lumen (*i.e.*, vessel wall-blood boundary). Technique performance was assessed using 3-fold cross validation with 15 cine FSE sequences per fold, each sequence consisting of 16 temporal bins across the cardiac cycle. The automatic segmentation was compared against manual segmentation results. Our technique achieved an average Dice coefficient, sensitivity and false positive rate of 0.926 ± 0.005 (mean $\pm$ standard deviation), 0.909 ± 0.011 and 0.056 ± 0.003 , respectively, compared to the voting consensus of three experts manual segmentation.

Keywords: max-tree, markers, tie-zone watershed, random forest, carotid, lumen, cineFSE imaging

Resumo

A aterosclerose é uma das principais causas de derrame cerebral e é responsável por milhões de mortes por ano. A ressonância magnética (RM) é uma maneira comum de avaliar a aterosclerose da artéria carótida. Um novo método de imagem de RM cine fast spin echo (FSE) agora pode obter dados de RM dinâmicos (*i.e.*, gerar imagens em todo o ciclo cardíaco). Este trabalho apresenta uma técnica de pós-processamento que automatiza a segmentação do limiar entre sangue e parede (lumen) da artéria carótida comum (ACC) ao longo do ciclo cardíaco. Até onde sabemos, este trabalho é a primeira técnica proposta para segmentar imagens cine FSE com resolução de ciclo cardíaco. A técnica supera algumas limitações da dinâmica em comparação com imagens estáticas (*ex.*, resolução espacial mais baixa). Ele combina o conhecimento *a priori* sobre o tamanho e a forma da ACC, com a estrutura de dados max-tree, classificador Random Forest e a transformada tie-zone watershed a partir de marcadores internos e externos para segmentar o lúmen do vaso. O desempenho da técnica foi avaliado usando validação cruzada com 3 folds com 15 sequências cine FSE por fold. Cada sequência consiste de 16 pontos de tempo em todo o ciclo cardaco. A segmentação automática foi comparada com resultados de segmentação manual. Nossa técnica alcançou um coeficiente dice, sensibilidade e taxa de falso positivo de 0.926 ± 0.005 (média $\pm$ desvio padrão), 0.909 ± 0.011 e 0.056 ± 0.003, respectivamente, em comparação com o consenso da segmentação manual de três especialistas.

Palavras-chaves:árvore máxima, marcadores, tie-zone watershed, floresta aleatória, carótida, lúmen, imagem Cine FSE

List of Figures

List of Tables

List of Acronyms and Notations

CC	Connected Component
CCA	Common Carotid Artery
CTA	Computed Tomography Angiography
DT	Decision Tree
ECA	External Carotid Artery
EM	External Marker
FPR	False Positive Rate
FSE	Fast Spin Echo
HOG	Histogram of Oriented Gradients
ICA	Interior Carotid Artery
IM	Internal Marker
LBP	Local Binary Pattern
LogR	Logistic Regression
MRA	Magnetic Resonance Angiography
MRI	Magnetic Resonance Imaging
RM	Regional Minimum
RF	Random Forest
SVM	Support Vector Machine
TZ	Tie-zone
VC	Voting Consensus

Contents

1 Introduction

1.1 Introduction

Stroke is one of the most common causes of death in the world. It is estimated that 4.4 million people die every year due to stroke and 5,000 in every 1,000,000 people suffer from stroke-related disability ((YUAN *et al.*, 2001)). Atherosclerosis is one of the main causes of stroke, causing about 25% of all ischemic events ((SAAM *et al.*, 2007)). Atherosclerotic vessel disease is characterized by accumulation of lipid, fibrin, cholesterol and calcium in artery walls, specifically at bifurcations and in regions of vessel curvature. Atherosclerosis progression is complex with severe cases resulting in complex plaques in the vessel wall and, eventually, a reduction in cross-sectional area (*i.e.*, the development of lumenal stenosis).

Currently there are several different types of exams to identify aterosclerotic plaques and analyze the carotid. The most used for determining carotid distensibility are ultrassound techniques, once they are lower cost (when compared with MRI), easier and with high temporal resolution. However these techniques have poor blood-wall contrast and calcifications contribute to create image shadowing ((BOESEN *et al.*, 2015)). On the other hand, x-ray techniques, such as computed tomography angiographys (CTAs) do not excel in tissue contrast ((MENDES *et al.*, 2011)).

Magnetic resonance imaging (MRI) is a technique that provides a great tissue contrast between vessel wall and lumen. Besides, it permits the evaluation of plaque morphology and composition, better defining the absence or presence of vulnerable (or "at-risk") carotid plaques ((YUAN *et al.*, 2001)) that can be treated medically (*e.g.*, statin therapy) or with surgery. (Figure [1])

For the development of this project we used Cine Fast Spin Echo (FSE) images, which differs from usual MR imaging for bring us dynamic information about distensibility and contraction of carotid artery through cardiac cycle. The method developed is applied on each slice individually, therefore we do not use the dinamic nature of the image for segmentation purposes. Despite the fact that usual MRI acquires images with a good tissue contrast, they usually have motion artifacts due the long time needed for acquisition ((MENDES *et al.*, 2011)). Cine FSE imaging, on the other hand, is capable of acquiring a number N of images (N between 10 and 20) during a cardiac cycle with the same time used by a standard FSE to acquire only one static image ((MENDES *et al.*, 2011; BOESEN *et al.*, 2015)).

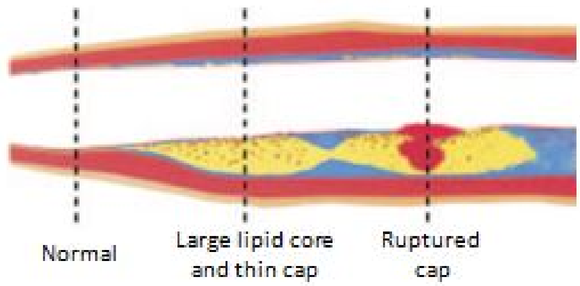

Figure 1 – Example of normal and vulnerable plaque (NAGHAVI, 2003).

1.2 Motivation

CCA lumen manual segmentation is not an easy task. It is time consuming and very subjective, specially in the limiar between lumen and CCA wall, which is the region most affected by the artifacts and blood flow, thus the most susceptible to be mistaken. Currently we can find in the literature many different methods of semi-automatic segmentation, however all of them have human iteration at some level.

Despite current image exams have good tissue contrast and good resolution, it is not common to find plaques in earlier stages ((NAGHAVI, 2003)). It is interesting to develop a non invasive, fast and robust method to quantify, monitor and assess carotid artery. Despite we do not use the dynamic information of cine FSE images for segmentation, one can analyze the elasticity of carotid artery and use this information to help identifying atherosclerosis disease in earlier stages. For so, we need the segmentation of CCA lumen as an initial step. Besides there are many studies on the literature presenting vessel lumen segmentation, as we will present on a later section, there is no technique proposing segmentation of dynamic images of vessels.

1.3 Objectives

This work is the first step of a larger project that intends to study carotid artery distensibility curves (CCA and bifurcation) and, based on them, classify patients as healthy or non-healthy. These curves are possible to be created due the dynamic nature of Cine FSE images, which will be explained on the next chapter.

Finally, the main objective of this work is the development of a fully automatic method to segment the lumen of Common Carotid Artery (CCA) using Cine FSE images. Since this is an initial project, to verify the viability of lumen segmentation on dynamic images, we will not focus on carotid bifurcation or plaque composition.

1.4 Bibliographic Review

Currently, we can find in the literature many articles concerning vessel lumen segmentation. There is a great variety of methods and types of images used, such as MRI, Magnetic Resonance Angiography (MRA), CTA, among others. In this topic, we will present some works developed, their methods and final result. In order to classify the studies, we will divide them into three larger groups, based on (LESAGE *et al.*, 2009):

- **Geometric models**: The segmentation is based on vessel shape.

  (ARIAS-LORZA *et al.*, 2016) created an optimal surface graph-cut algorithm to segment the carotid wall bifurcation on MRI with minimum user interaction. To do so, they also segment the lumen. The method is based on three main steps: At first, the image is pre-processed and three seed points are manually chosen. Then, centerlines are computed and the lumen is coarsely segmented by centerline dilatation. As second step, a surface graph is constructed and finally the minimum graph cut is computed. To validate the method the authors used 31 unhealthy subjects. To compute the centerlines Black Blood MRI (BBMRI) and Proton density weight MRI (PD-W MRI) images were used. They achieved a dice coefficient of 0.89 ± 0.09 for lumen segmentation and 0.86 ± 0.06 for complete vessel.

- **Appearance models**: Based on luminance properties, depend on the imaging modality.

  (UKWATTA *et al.*, 2013) proposed a multi-region segmentation method, partitioning the image into lumen, outer wall and background. In order to do so, they compute the lumen intima boundery (LIB) and carotid adventia boundery (CAB). To do so, they utilize the Probability Density Function (PDF) of intensities (i.e. intensity histogram) as global descriptor. The two surfaces CLIB and CAB are then propagated to their PDF models using the minimal Bhattacharyya distance. Finally, they end up in an optimization problem for the simultaneous evolution of the two surfaces. This problem is globally solved using convex relation and introducing a new continuous max-flow-based algorithm. The method is done with minimal user interaction. It is needed to choose a few voxels of carotid wall, lumen and background on one single transverse slice. The authors used two different datasets, the first one was composed by 12 T1W 3T MRI images, in which they found a dice of $93.3\% \pm 1.4\%$ for LIB and 93% for AB and the second dataset composed composed by 26 T1W 1.5T MRI images, in which they got a dice coefficient of 91.3% ± 1% for CAB and 92.4% ± 2.1% for LIB

- **Hybrid models**: Combine appearance and geometric models.

  (LOPEZ V.NARANJO, 2011) segmented the aorta artery in MRI images. They developed a semi-automatic algorithm based in mathematical morphology and watershed transform. To do so, they process the 3D MRI image slice by slice. The image is pre-processed with morphological filters and for segmentation they choose two markers, internal and external to aorta artery, to be used as input to the watershed transform. The internal marker is chosen as the geodesic center of the descending aorta and external marker is the dilation of this point by a structuring element of n=30. The first point is selected by the user. As result, they find a Jaccard coefficient of 0.81 ± 0.02 and a Dice coefficient of 0.878.

  (SAKELLARIOS *et al.*, 2012) proposed a luminal border, outer vessel wall detection and plaque composition characterization. They used 1.5T MRI images performed in 24 patients. As pre-processing, they perform an image cropping, contrast enhancement and media filtering, The next step is the luminal border detection, done in axial TOF MR images. First they find a coarse segmentation using Otsu's method. Then, Canny technique is applied for edge detection. With the result of this step, a 3D volume is generated and an in-house 2D clearing algorithm is used to eliminate points that are not classified as luminal borders. For the first image, seeds need to be identified by the user. For bifurcation, they use connected components theory, assuming that CCA is one large component and internal carotid artery (ICA) and external carotid artery (ECA) are two different components of comparable sizes. Finally, active contour is used to detect the final borders of CCA, ICA and ECA. For plaque characterization, they use a three-level decision tree for classification and fuzzy c-means for categorization of the plaque. They found a variability for lumen and outer vessel wall of -1.6± 6.7% and 0.56 ± 6.28 %. Dice coefficient was not reported.

After studying the existing work of vessel segmentation found on the literature, we could notice that there is no consensus about the method. Since the authors differ in relation to the tools, there is no solidified method as the best to use for solving the problem of lumen segmentation of vessels and arteries such as the carotid artery. Therefore, we have created a new method that could best fit our type of images, which also differ from the ones found in the literature due to its dynamic nature.

In the present work, a hybrid model was used in Cine Fast Spin Echo (Cine FSE) time-series of MR images with the goal of finding a robust pattern of the carotid surface area. Each MR time-series volume is composed of one sequence of 16 temporal bins that compose a period of a cardiac cycle. Our method uses the max-tree (SALEMBIER *et al.*, 1998; JONES, 1999) with tie-zone watershed (LOTUFO *et al.*, 2002) and random forest classifier (BREIMAN, 2001) to get accurate segmentations.

1.5 Organization of the dissertation

This dissertation is organized as follows: Chapter 2 presents a brief theoretical background concerning max-tree, watershed, cine-FSE images, Random Forest, features descriptors, such as HOG and LBP, and the metrics used to assess the method. Chapter 3 explains the method developed for automatic CCA segmentation. Chapter 4 presents the method results and ground truth used and discuss the results. Also, we show a best case scenario using the Tie-Zone Watershed Transform and make a few changes on the code to analyze each one of the proposed steps. Chapter 5 presents the conclusions, future work and a publications list related to this research.

2 Theoretical Background

In this chapter, it is presented a brief theoretical background about Cine FSE Images, Max-Tree, Watershed, Random Forest and some feature descriptors and metrics used in our methodology.

2.1 Cine FSE Images

Conventional static MR imaging techniques generate images with acceptable vessel wall-blood image contrast and allow for the depiction of vessel wall morphology and characterization of plaques components. FSE images, with proton density-, T1- and/or T2-weightings are commonly used ((SAAM *et al.*, 2007; YUAN *et al.*, 2001)). These images provide only a snap-shot (time averaged) of the vessel wall morphology and composition over the cardiac cycle. They can also suffer from cardiac motion-induced artifacts due to their long data acquisition times ((MENDES *et al.*, 2011)). Cine FSE imaging is a new technique that is capable of acquiring images across the cardiac cycle in total acquisition times similar to those required for a standard static FSE technique, albeit often with reduced spatial resolution ((BOESEN *et al.*, 2015; MENDES *et al.*, 2011)). Because cine FSE images are resolved over the cardiac cycle they potentially can reduce image artifacts due to motion(BOESEN *et al.*, 2015).

Cine FSE acquires data over the entire acquisition window asynchronously with respect to the contraction of the heart. The acquired raw MR data is however tagged with its acquisition time within the cardiac cycle (typically using information from a pulse oximeter). The raw data is then rebinned into N temporal bins that evenly cover the average cardiac cycle. N is user selectable and typically is between 10 and 20. Because the raw MR data was collected asynchrounoulsy, each rebinned data set will, in general, be incomplete. Therefore sophisticated, non-linear reconstruction methods, based on compressed sensing ((LUSTIG *et al.*, 2007)), are required to generate images. Compared to static FSE images, cine FSE images are able to generate a similar range of image contrasts (weightings), with potentially lower resolution and signal-to-noise, but fewer motion artifacts. For this project, we used sequences of images rebinned into 16 temporal bins, as we can see on Figure 2. The cine FSE data acquisition process is fully explained in (BOESEN *et al.*, 2015).

The major differences between the usual MR acquisition and Cine FSE images are image contrast, resolution and motion artifacts. Usual MR has better contrast and resolution, while Cine FSE is faster and deals with motion artifact problems (Figure 3).

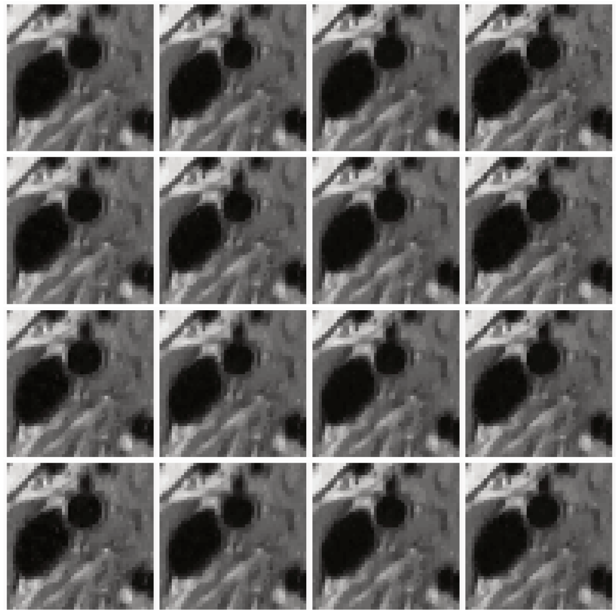

Figure 2 – Sequence of 16 temporal bins of the same slice during the cardiac cycle (zoom in around a CCA) collected with Cine FSE technique.

(a) 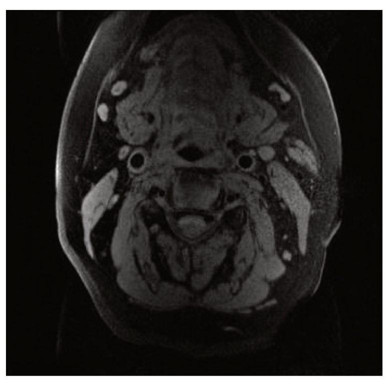 (b) 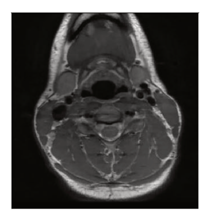

Figure 3 – Examples from different patients: (a) Static MR Image. (b) Cine FSE Image.

2.2 Image Representation

We can define an image I as a function f(x,y), where x and y are the coordinates and the amplitude of f in a given pair of coordinates is its gray level.

An upper threshold of a gray-scale image results in a binary image, where each pixel with a value greater or equal to the threshold receive the value 1 (white) and all other pixels receive value 0 (black). Loosely speaking, a binary image is composed of "islands", which in image processing are called connected components (CCs) ((SOUZA *et al.*, 2014)).The CCs have an inclusion relationship, the higher the threshold value the smaller the component will be, and it may even split in two or more components (Figure 4).

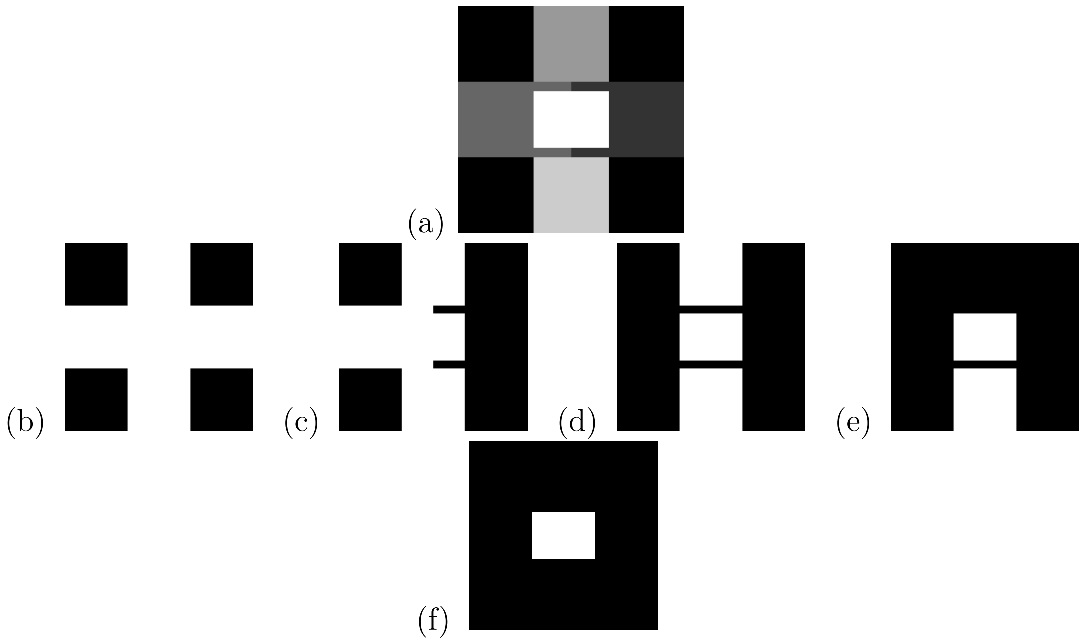

Figure 4 – Connected components for different threshold (T) values (a) Original Image I. (b) I > 0 (c) I > 1 (d) I > 2 (e) I > 3 (f) I > 4

2.2.1 Component Tree

Before defining the component tree, we need to introduce the definition of a node: A node is an abstract representation of the CCs, keeping information as gray level, attributes values, area, eccentricity, perimeter ((JONES, 1999)). The Component Tree is a set of nodes, each one representing a particular CC. It represents the image according the gray level of the CC.

Figure 5(b) represents the construction of component tree corresponding to a 1D sequence (Figure 5(a)). As we can see, the first CC, also called root, represent the entire image as a superset of all the CCs. As we analyze the component tree, we can observe that all nodes are linked to each other at a higher gray level with exception of one node. This node is called the regional maximum. The pixels around a regional maximum will always have a lower gray level than it.

2.2.2 Max-Tree

As we said before, for the component tree, the nodes are representations of the CCs. This means that all the pixels of the CCs are represented in the node and all the CCs will be represented on the Component tree. Therefore, sometimes for different thresholds, we will have the same CC, which causes redundancy to the model. In order to create a more compact version of the component tree, ((SALEMBIER *et al.*, 1998)) presented the definition of the Max-tree. Each node of the max-tree represents a different connected component resulting of an upper threshold. Loosely speaking, the max-tree nodes stores only the pixels that are visible at the image. The nodes that remain unchanged for a sequence of thresholds are called composite nodes. We can see on Figure 5(b) the max-tree construction of a 1D sequence.

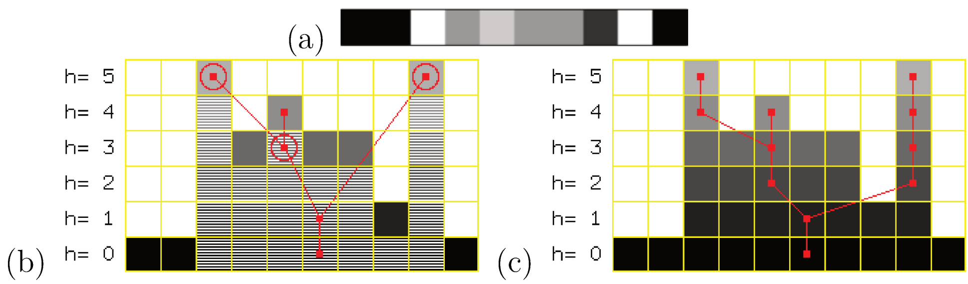

Figure 5 – (a) 1D sequence image representation (b) Component Tree for 1D image (c) Max Tree for 1D Image

The max-tree creates the image decomposition based on the higher threshold, this means that by using a max-tree we are interested on the brighter areas of the image. If we are interested on the dark areas of the image, we should use the min-tree instead. The min-tree follows the same structure of the max-tree, with the difference that its composition is based on the lower thresholds. In other words, if we want the min-tree of a given image I, we basically need to construct the max-tree of the negative of I.

Many attributes, such as area (volume), bounding-box coordinates, extinction values and others, can be extracted from the max-tree nodes, for tasks like object recognition and segmentation ((SOUZA *et al.*, 2014)). The max-tree computation, extraction of different attributes and filtering can be computed very fast silva08. A simplified illustration of the max-tree of a carotid image is depicted in 6.

2.2.3 Max-Tree Signature

The max-tree signature consists of analyzing the variation of an attribute of any pair of nodes connected by a max-tree path. It conveys information concerning the variation in shape and/or size of a connected component. The attribute signature uses the linking information between connected components at sequential gray-levels in the image to help the decision making process. Figure 7(b) shows us the area signature of input image (Figure 7(a)) negative, starting in a node inside the carotid (highlighted in green) and ending at the

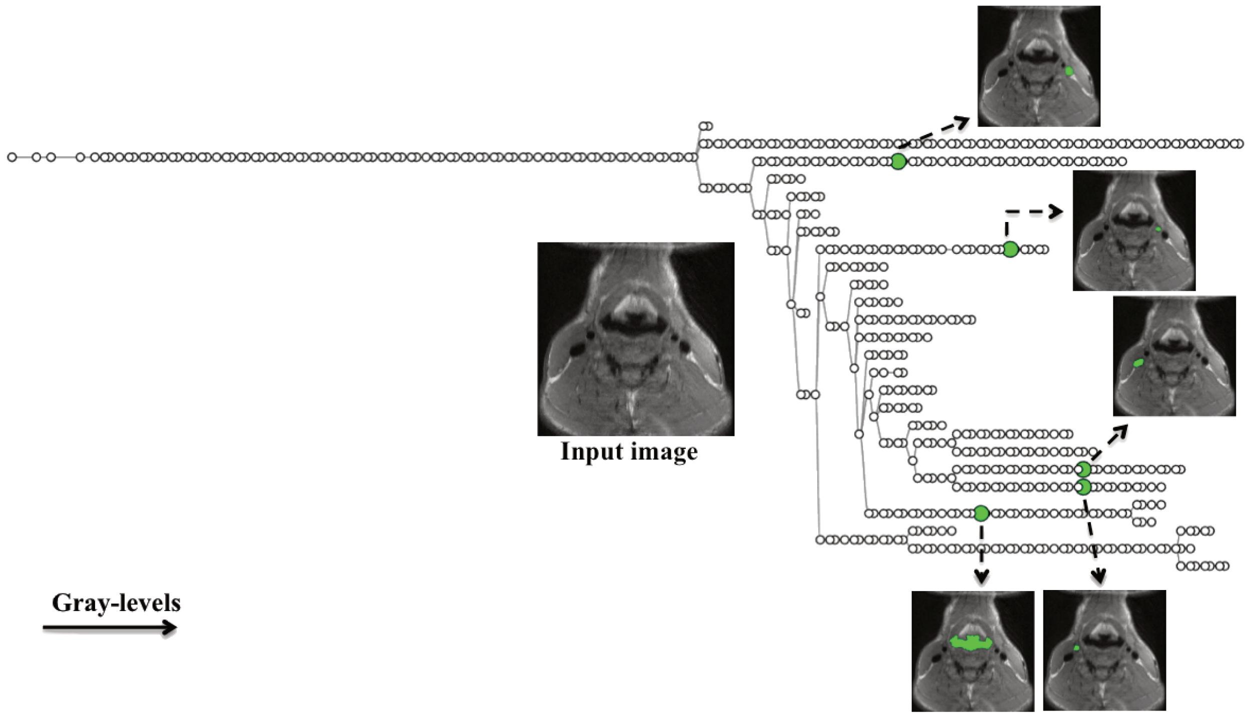

Figure 6 – Max-tree nodes illustration of a sample carotid image. The nodes represent connected components for each gray level. Some nodes, in green, are represented on images.

max-tree root. We can see that for higher thresholds the carotid lumen starts to separate itself from the rest of the image.

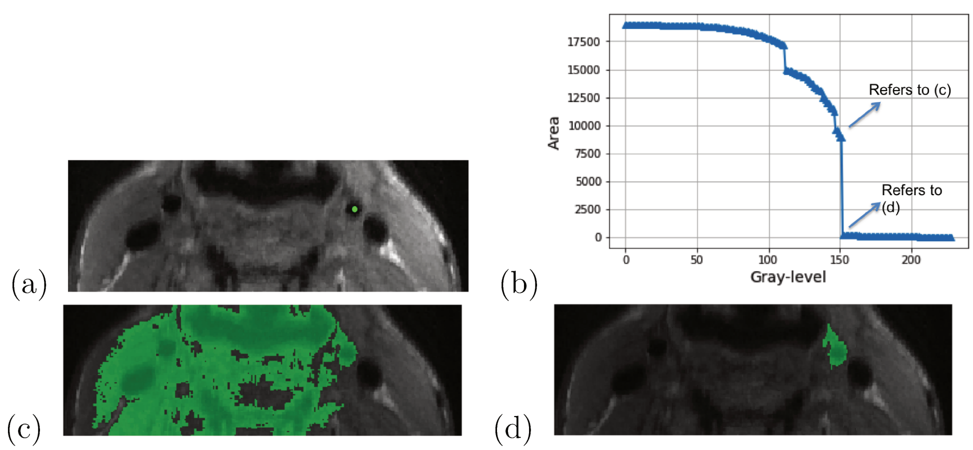

Figure 7 – Max-tree area signature analysis: (a) carotid image with seed point highlighted in green. (b) Area signature starting at the node corresponding to the seed. (c) Node reconstruction at gray-level 151. (d) Node reconstruction at gray-level 152.

2.3 Watershed

The watershed method considers the image as a topographic surface based on flooding simulation. Regional minimum (RM) are the origin of a flooding that increases until water from different RM start to merge. By this time, a dam is created to avoid the waters to merge, as we can see on Figure [8]. The final segmented image is composed by the watershed lines, represented by the visible dams above the waterline. We call catchment basin the resulting areas flooded from one RM ((DOUGHERTY; LOTUFO, 2003)).

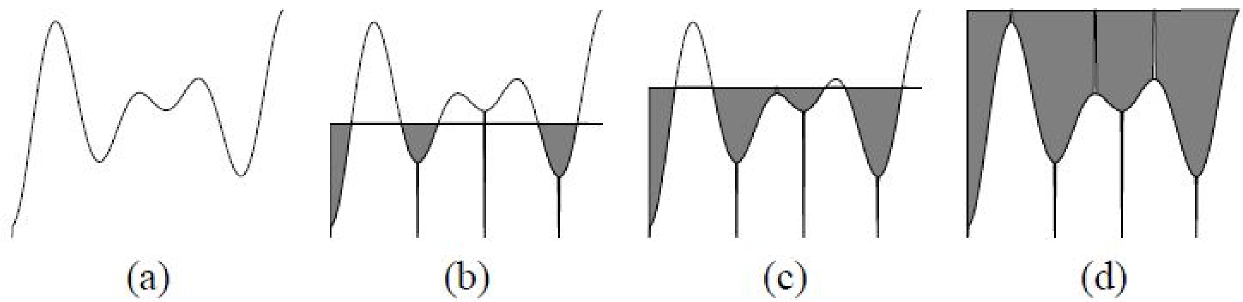

Figure 8 – Watershed ((DOUGHERTY; LOTUFO, 2003))

Usually, watershed is applied on the gradient image, however the gradient is composed by numerous regional minimum. This characteristics of the image leads to over-segmentation, this means, the final result will have more damns than the expected, as we can see on Figure 9(c). To avoid this, we use the watershed from markers.

2.3.1 Watershed from markers

To avoid over-segmentation, we can use watershed from markers. In this case, the flooding simulation is done with a small change: We punch holes on the markers regions. Now, the flooded water will be colored, each color representing one marker. Different of the watershed without markers, in this case a dam will be created only when waters of different colors begin to merge, minimizing the number of Watershed lines ((DOUGHERTY; LOTUFO, 2003)). This process is represented on Figure [10]. Although this case lowers the over-segmentation, the markers extraction needs to be done carefully and precisely. Usually we have markers for the background and markers for the foreground. If a marker is not well placed or if it is missing, a part of the segmentation will be compromised, as we can see on Figure 11].

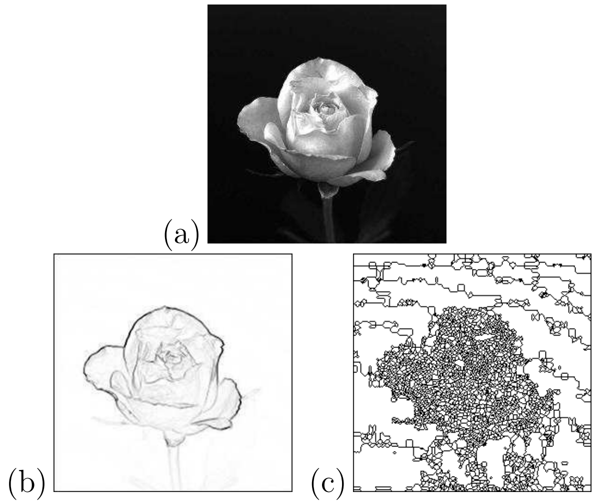

Figure 9 – Watershed Segmentation Example (a) Original Image I (b) Gradient Image of I (c) Watershed lines for I

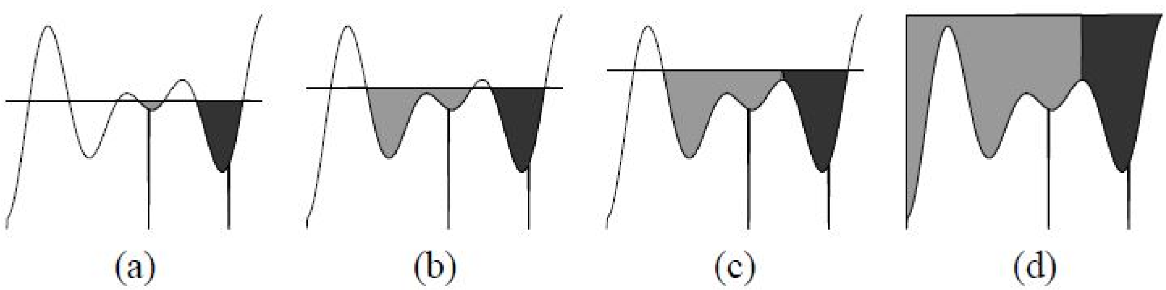

Figure 10 – Watershed from markers Dougherty03

2.3.2 Tie-Zone Watershed

The watershed transform from markers can be seen as an optimization problem. (AUDIGIER *et al.*, 2005) showed that the watershed transform may have multiple solutions, and its output may depend on algorithm implementation details, such as the order the image pixels or pixels neighbors are processed (Figure 12). For instance, the watershed result applied to an image can be different of the watershed result applied to the same image rotated by 90°, which is an undesirable feature. The tie-zone watershed ((AUDIGIER *et al.*, 2005)) assigns a tie-zone label to the regions that have the same cost to more than one marker. The tie-zones regions then may be addressed in a subsequent post-processing step.

The tie-zone watershed from markers applied to a carotid MR image is illustrated in Figure 13. Two markers are used in this case, one internal marker in the carotid lumen and

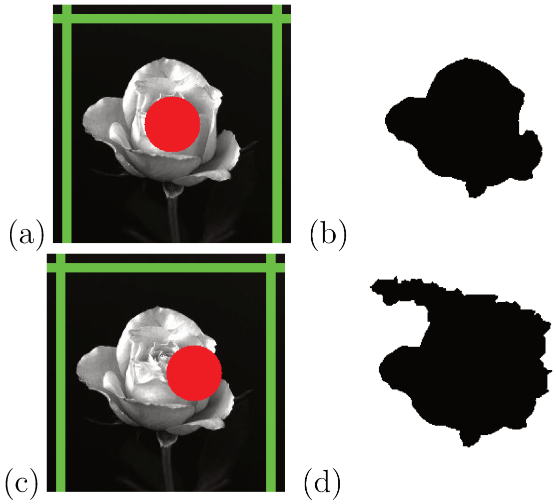

Figure 11 – Watershed from markers, avoiding over segmentation (a) Inner (red circle) and Outer (green lines) markers for watershed segmentation correctly placed (b) Final segmentation as expected (c) Inner (red circle) and Outer (green lines) markers for watershed segmentation wrongly placed (b) Final segmentation presenting leakage

Figure 12 – Illustration of the tie-zone watershed from markers. Depending of the implementation, different solutions can be found. In this case, the middle pixel was assigned as A and as B on two different approaches. This pixel represents a tie-zone.

one external marker on the carotid wall. In this example, the area of the pixels segmented as lumen corresponds to 63 pixels, while the tie-zone area is of 64 pixels, which shows that the tie-zones have significant influence on the segmentation results.

2.4 Random Forest Classifier

2.4.1 Decision Trees

Decision Tree (DT) is a classifier based on nodes and edges structure, designed to deliver a decision about a certain attribute vector V ((CRIMINISI; KONUKOGLU, 2012)). A DT structure is shown on Figure [14](a).

DT nodes can be divided into split nodes, that will store the test function and the leaf nodes, which will store the final prediction. To construct the tree, we use the training

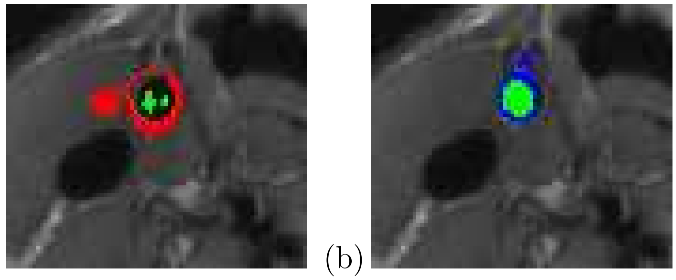

(a) (b)

Figure 13 – Illustration of the tie-zone watershed from markers. (a) Internal (green) and external (red) markers. (b) Tie-zone watershed result with the tie-zones shown in blue.

data to create a optimization function in each of the split nodes. Each split node represents a class histogram, and we can determine the probability of a certain test sample to be of a class S based on the node histogram Figure [14](b),(c),(d).

Being X a dataset containing a number N of different classes, we can do more than one split to classify the samples. Depending on the split,we can optimize the prediction and achieve a better accuracy on the classifier. In Figure [15(a)] we have a dataset containing two different classes. If we trace two different lines to split it, we can see that a vertical line Figure [15(b)] will work better for splitting the dataset correctly than an horizontal line Figure [15(b)]. Those lines are the representation of the function used by the nodes to split the data. Those functions, or criteria, are better explained on the next section.

2.4.2 Entropy and Information Gain

The entropy measures the uncertainty of a given random experiment. The more uncertain the result of a random experiment, the greater the information obtained by observing its occurrence.((CRIMINISI; KONUKOGLU, 2012)). For a better split of tree nodes, we look for a reduction on the entropy, also known as Information Gain (IA). In other words, the attribute with higher IA will be the better one to describe a given dataset. The Information Gain and Entropy can be defined as shown on Equations (2.1) and (2.3), respectively.

$$I(A) = H(\frac{p}{p+n}, \frac{n}{p+n}) - EH(A) \tag{2.1}$$

$$H(\pi) = -\sum \pi log \pi \tag{2.2}$$

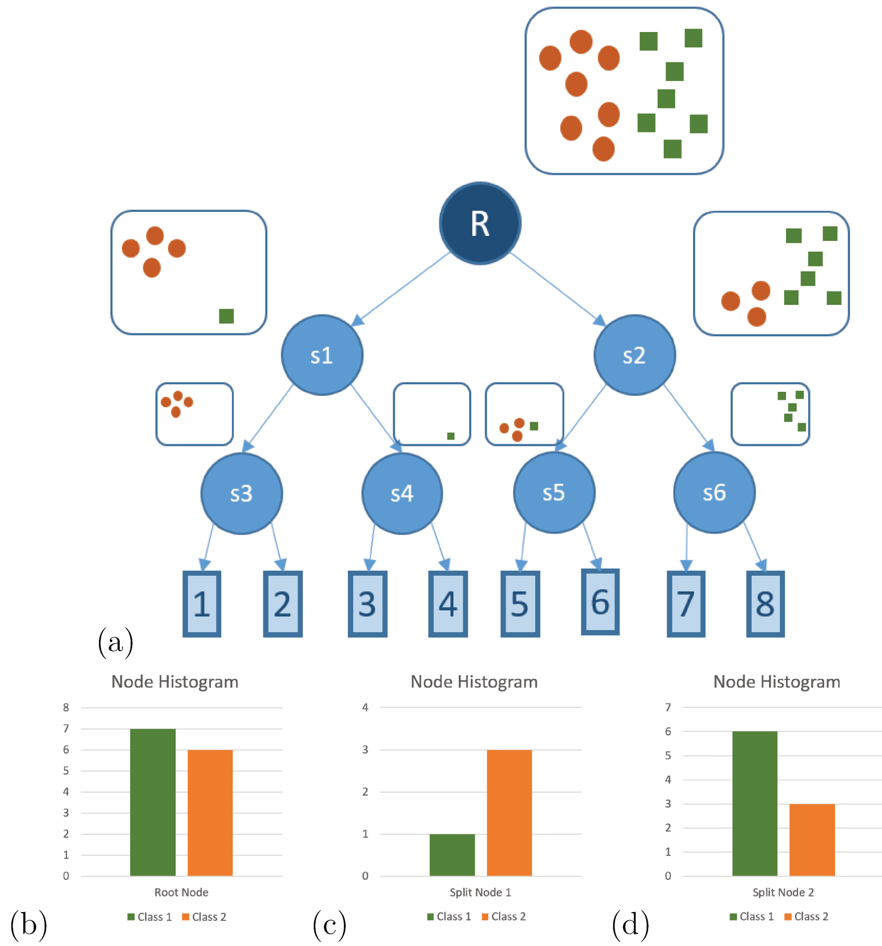

Figure 14 – Decision Tree example (a) DT architecture (b) Histogram of classes for split node 1(c) Histogram of classes for split node 2 (d) Histogram of classes for split node 3

$$EH(A) = \sum_{i=1}^{k} \frac{p_i + n_i}{p + n} H\left(\frac{p_i}{p_i + n_i}, \frac{n_i}{p_i + n_i}\right) \tag{2.3}$$

2.4.3 Random Forest

Random Forest, as the name implies, is an ensemble of decision trees (Figure [16])

All the DT are trained in parallel and independently with bootstrap aggregation, which reduces the correlation between them. The final classification is done based on the vote of all tree predictions ((BREIMAN, 2001)). Being (v) a datapoint inserted through a random forest containing T predictors (DTs), the final prediction of the classifier for (v) will

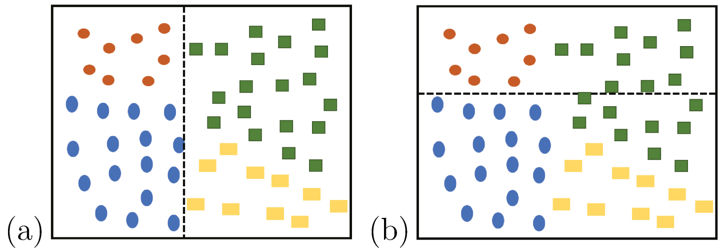

Figure 15 – Dataset X (a) Example of splitting line (b) Example of vertical splitting line, which works better for this example

be:

$$p(c \mid \mathbf{v}) = \frac{1}{T}\sum_{t=1}^{T} p_t(c \mid \mathbf{v}) \tag{2.4}$$

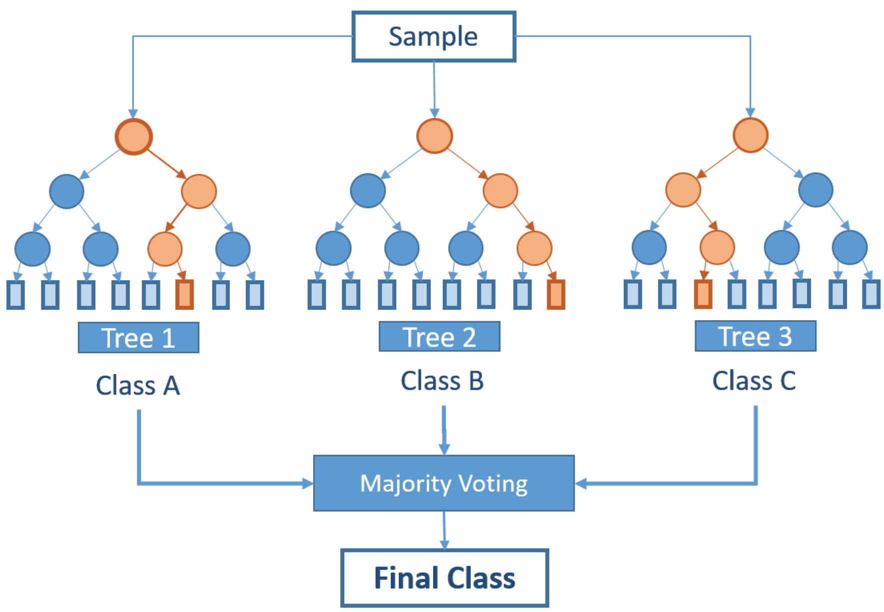

Figure 16 – Random Forest architecture

2.5 Feature Descriptors

2.5.1 Local Binary Pattern

Local Binary Pattern (LBP) is a texture descriptor commonly used in different applications such as objects recognition.

As can be seen on Figure [17], LBP operates by passing a 3x3 window through the imaging and thresholding the window values based on the centered pixel. The result can be analyzed as a binary number that can also be converted to a decimal number ((AHONEN A. HADID, 2006)).

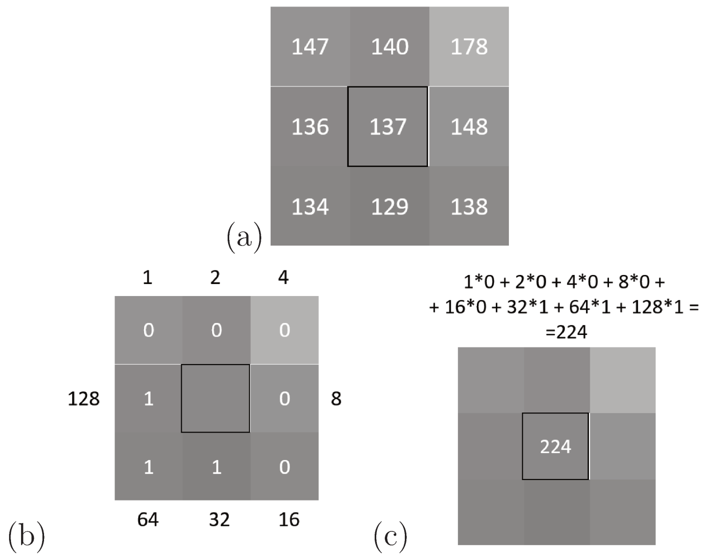

Figure 17 – Linear Binary Pattern (a) Example of 3x3 image (b) Step 1: neighbor pixels are set to 0 when they are greater or equal than the center pixel and set to 1 when they are smaller than the center pixel (c) We find the final value based on the LBP values

A LBP image can be seen on Figure [18].

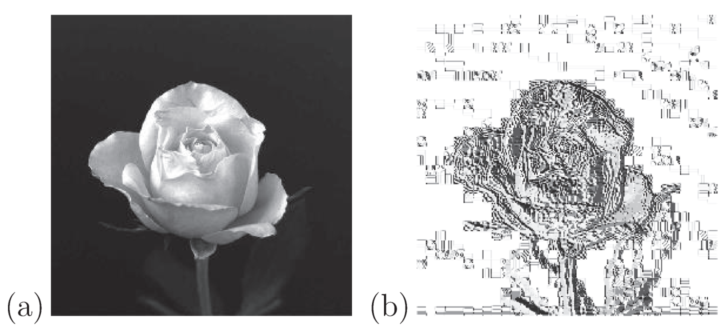

Figure 18 – Linear Binary Pattern (a) Original image (b) LBP image

2.5.2 Histogram of Oriented Gradients

The histogram of oriented gradients (HOG) is a feature descriptor widely used for human and object detection. It was first proposed by ((DALAL; TRIGGS, 2005)) and it is based on the image gradients, as the name suggests. At first, we calculate the horizontal (g_y) and the vertical (g_x) gradients of the image. Using (g_x) and (g_y) we can find the final magnitude (g) and direction Θ of the gradient by the equations bellow:

$$g = \sqrt{g_x^2 + g_y^2}$$

$$\Theta = arctan \frac{g_x}{g_y}$$

Looking at Figure [19](c)(d), we can see that x-gradient is more intense on the verticals lines, while the y-gradient is more intense on the horizontal lines. The final magnitude is stronger where the change of intensity is more abrupt. None of them is fired on smoother regions, like the backgroung.

Briefly speaking, we can assume that the gradient image highlight all the essential information (*e.g.* edges) and removes the non-essential (for instance, the backgroung). The magnitude and direction of HOG are interpreted in Figure [19](b). As we can see, the arrow points the direction of the intensity change, while the magnitude indicates how big this change is.

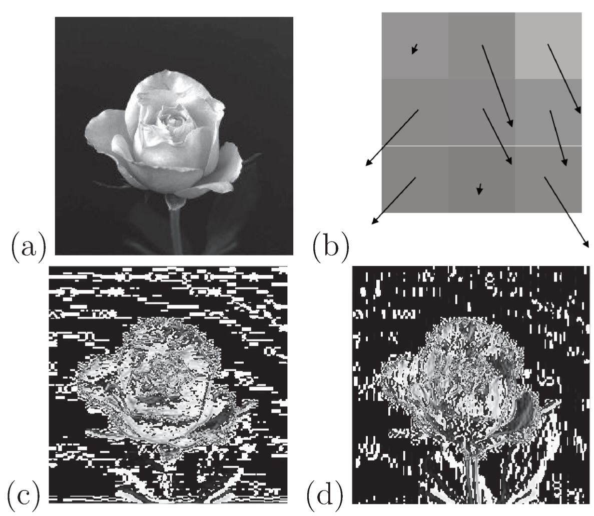

Figure 19 – Histogram of Oriented Gradients (a) Original Image (b) Direction and magnitude of each pixel of 3x3 window (highlighted in red on (a)) (c) Gy (d) Gx

Finally, as the name suggests, HOG is a histogram, so to calculate it we will summarize the magnitude information of the image on a 9 bin vector, representing the directions.This process is better explained in Figure [20].

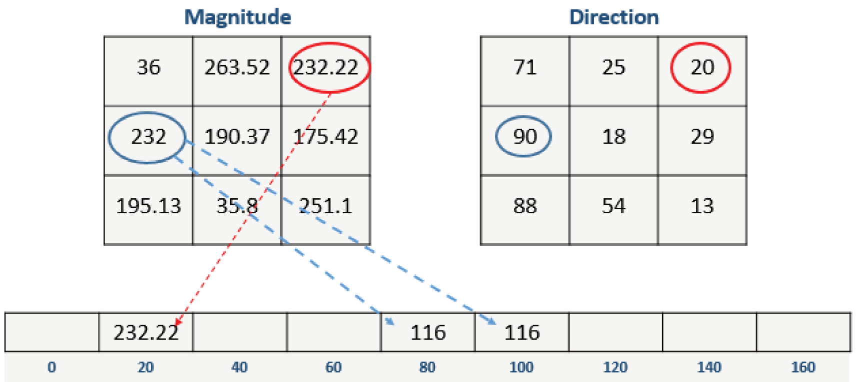

Figure 20 – To calculate HOG we need to analyze the magnitude and direction of the pixel. In this image we have an example of magnitude and direction of the 3x3 window from Figure [19](a). For instance, we have circled in red a pixel with direction of 20º and magnitude of 232.22. In this case, we add the whole magnitude value on the histogram bin equivalent to direction 20º (Second bin). For the blue circled pixel, the direction is 90º. We do not have a bin representing this direction, so we divide the magnitude of this pixel proportionally into the 5th and 6th bins (80º and 100º).

2.6 Metrics

Suppose that G is the ground truth image and S is the segmentation we want to assess, the metrics used to evaluate the method are given by the following equations:

- Dice coefficient:

$$Dice(G, S) = \frac{2|S \cap G|}{|S| + |G|}$$

- Sensitivity:

$$Sensitivity(G, S) = \frac{|G \cap S|}{|G|}$$

- False positive rate:

$$FPR(G, S) = \frac{|G^c \cap S|}{|G|}$$

The Dice coefficient can be viewed as a compromise between sensitivity and specificity and is probably the most widely used metric to assess segmentation. Sensitivity measures how much brain tissue is included in the segmentation. The FPR gives the fraction of false positive results as a percentage of the ground-truth size. The larger the Dice coefficient and the sensitivity the better is the quality of the segmentation; while the smaller the FPR, the better is the segmentation.

In order to assess the performance of classifiers, the following metrics were used:

- Precision

$$precision = \frac{tp}{(tp + fp)} \tag{2.5}$$

- Recall

$$recall = \frac{tp}{tp + fn} \tag{2.6}$$

- F1-Score

$$F1 - Score = \frac{2 * (precision * recall)}{(precision + recall)} \tag{2.7}$$

Being tp, fp and fn true positive, false positive and false negative, respectively. They can be define on Table 1, also known as confusion matrix for binary cases.

Table 1 – Confusion Matrix for binary cases

	Predicted Class 0	**Predicted Class 1**
Actual Class 1	TP	FN
Actual Class 0	FP	TN

Precision defines the correct predictions rate for a given class within all the predictions, that is, the ones that were relevant. In other words, the proportion of predictions that were correctly classified among all the predictions.

Recall is defined by the correct predictions rate within a given class, that is, a proportion of relevant labels that have been predicted.

F1-score is the weighted average between precision and recall. It varies from 0 to 1, being 1 the best result one could achieve.

2.7 Chapter Conclusions

This chapter presented the minimal theoretical background necessary for the development of subsequent chapters. More detailed and formal definitions can be found on cited bibliography.

3 Common Carotid Artery Lumen Segmentation

In this chapter we will present the developed method for CCA lumen segmentation. Our solution uses appropriate size and shape information obtained from the max-tree algorithm to find CCA centroid, internal and external (to the carotid artery lumen) markers that then are used by the tie-zone watershed transform. The max-tree is a good tool for finding structures of the image that present an important gray level difference among their neighbours. For internal and external markers we find nodes on lumen and vessel wall, this means, dark and bright structures, respectively. The proposed method developed has five main steps detailed below (Figure 21).

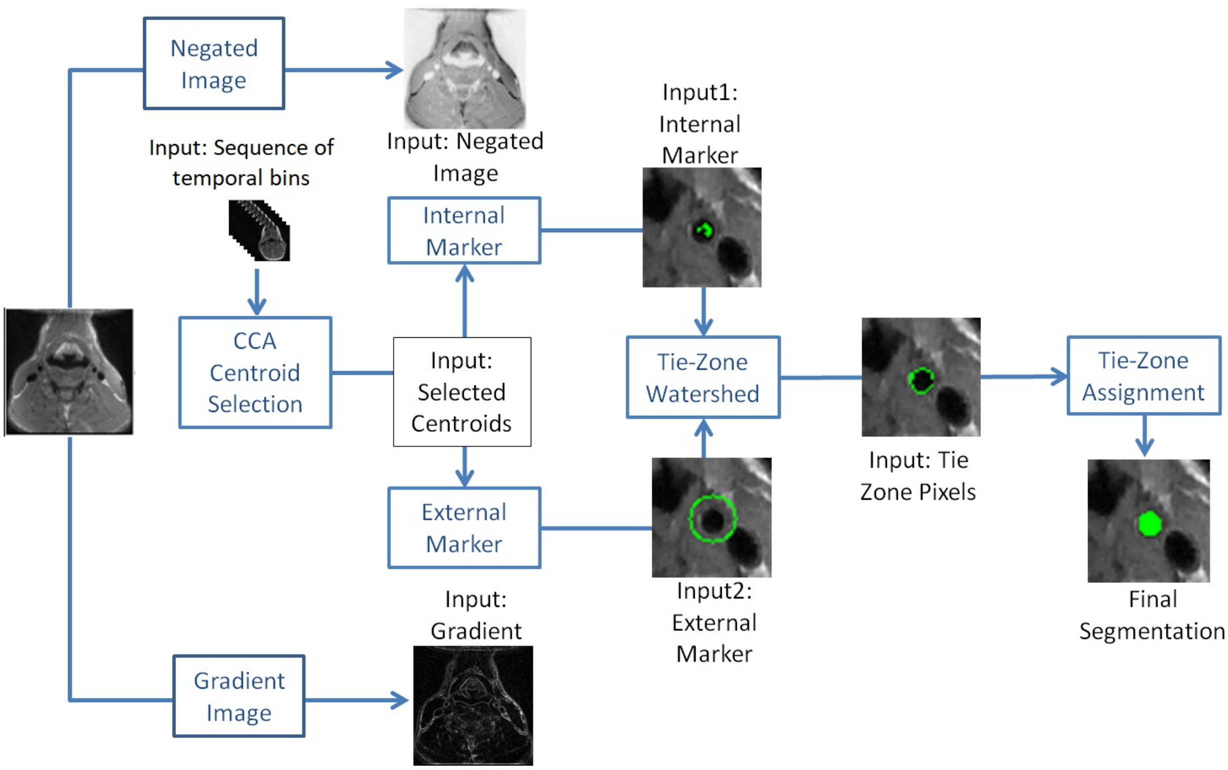

Figure 21 – Flowchart of our proposed method.

Initially, we automatically select CCA centroid. This selection is done using max-tree filtering and random forest classification. Using the selected centroids, we build the max-tree of negated image and gradient image. Those will deliver us an internal an external marker, respectively. The markers will feed a tie-zone watershed transform. Finally, we perform a classification on the tie-zone pixels and get the final segmentation. All the steps of the method are better explained bellow.

3.1 CCA Centroid Selection

The first step of the method requires the automatic selection of the left and right CCA centroids, detailed on Figure 22. For so, we used max-tree for image filtering and feature extraction and random forest classification for final selection.

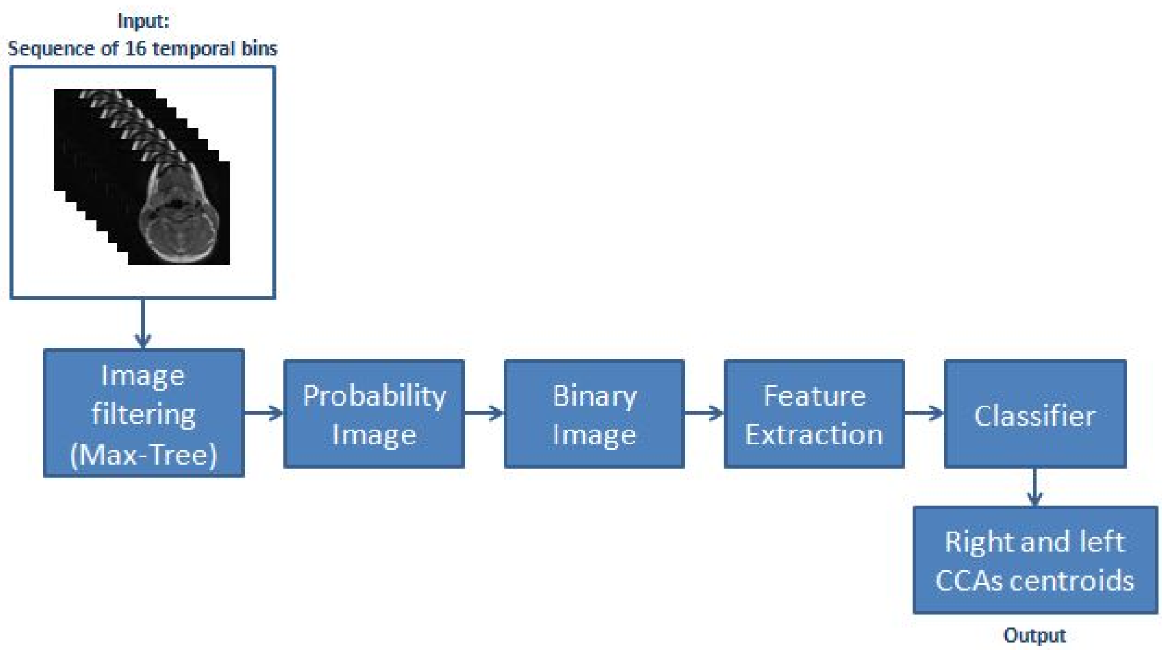

Figure 22 – Flowchart of CCA centroid Selection algorithm

- Max-Tree Filtering

  For this first step, we have as input an entire sequence of cine FSE images, this means, all 16 temporal bins. Initially, we use a max tree filter to return only the nodes with area between 14.5mm^2 and 46.6mm^2, once CCA areas are well established from measurements in the literature (diameters ranging from 4.3 mm to 7.7 mm) ((LIMBU *et al.*, 2006)). This filter is used on all 16 temporal bins of the sequence.

- Probability Image and Binary Image

  A probability image is created by summing all 16 filtered images of the previous step. Then we apply a threshold of 0.8 on the probability image, maintaining only pixels that appear in more than 80% of the images (Figure 23). After this step, our output will be a binary image containing the candidate nodes for CCA.

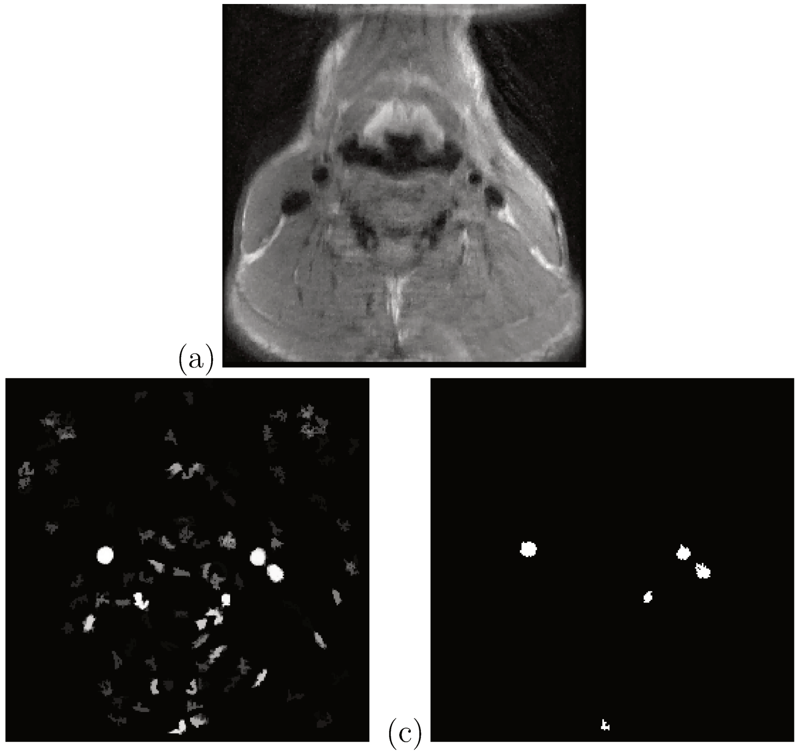

(a) (b) (c)

Figure 23 – (a) Original image. Here is shown only one of the 16 temporal bins used on this step of the method. (b) Probability image generated from the sum of all 16 temporal bins after max tree filtering (c) Final binary image containing only pixels that appear in more than 80% of the images

- Feature extraction

Using the final binary image, seen in Figure 23(c), we perform the feature extraction for each node candidate of the image. The attributes analyzed here are:

- *Gray level:* The vessels are the darkest structures of the image

- *Area:* CCA has an area ranging between 14.5mm^2 and 46.6mm^2

- *Eccentricity:* CCA has a circular shape

- *Centroid of remaining structures and Distance between remaining structures:* Right and left CCA maintain a symmetric appearance

In order to create a feature matrix, we divide the final image in left side and right side and analyze the structures by pairs. A better explanation can be seen on Figure 24 and Table 7. By the end of this step, we have a feature matrix of dimension Nx11, being N the number of candidate pairs returned in the image.

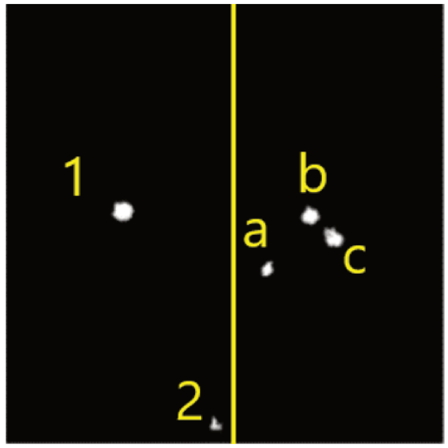

Figure 24 – Binary Image used to extract features. We analyze it by pairs, dividing the image in right and left sides. In this case, we have six pairs. We are interested in detecting the pair 1-b.

Table 2 – Feature matrix for Figure 24. (A = Area; Ecc = Eccentricity; Cent = centroid coordinates of structure; R = Right side; L = Left side)

Pair	**AR**	**AL**	**EccR**	**EccL**	**CentR**	**CentL**	**glvR**	**glvL**	**Distance**	**Label**
1-a	98	36	0.891	0.415	[120,68]	[154,153]	10	8	91	0
1-b	98	69	0.891	0.950	[120,68]	[123,178]	10	7	109	1
1-c	98	78	0.891	0.527	[120,68]	[136,191]	10	11	124	0
2-a	24	36	0.466	0.415	[244,122]	[154,153]	27	8	96	0
2-b	24	69	0.466	0.950	[244,122]	[123,178]	27	7	134	0
2-c	24	78	0.466	0.527	[244,122]	[136,191]	27	11	129	0

- Classifier

  In this step, we used a Random Forest (RF) classifier, explained on Chapter 2. As input for the RF we use the feature matrix generated on the previous steps. Our final classifier was a Random Forest with 45 estimators, operating with entropy criteria. The classifier input will be the feature matrix found on last step (Table 7). As output, we have the pair of centroids with highest probability of being left and right CCA.

3.2 Internal Marker Selection

The Internal Marker (IM) selection is done based in a priori knowledge of carotid artery area and one assumption about cine FSE images, which are:

- The Carotid diameter varies from 4.4mm to 7.7mm (LIMBU *et al.*, 2006)
- The histogram of two consecutive temporal bins are similar, as we can see on Figure 26. If we compare the first bin of the sequence with the last one, we can see a higher

discrepancy between histograms then comparing the first and second bins, *ie*, the peaks of histograms of consecutive temporal bins are closer than peaks of histogram of non-consecutive temporal bins..

For selecting the (IM) we are interested in the carotid lumen which is a dark point of the image. At first, we build the max-tree of the negative of the input image (min-tree), then, we analyze the max-tree area signature starting from the selected centroid all the way down to the max-tree root. Then, we create a filter using the previous knowledge about CCA area, reducing the number of max-tree nodes that need to be analyzed. We can see on Figure 25 that after the signature fall we only have nodes representing the carotid, both lumen and vessel wall. Among those, we need to find the internal marker.

From the final candidate nodes, the IM is selected based on our histogram assumption. We select as an internal marker the candidate with gray-level value closest to the gray level of the previous temporal bin. For the first temporal bin, we select the node with gray level closest to the highest peak of the histogram, once the vessels are the darkest structures of the image.

3.3 External Marker Selection

For external markers (EM), we are interested in the vessel wall, which is the brighter structure around the lumen. For so, we built the max-tree of the gradient image to find nodes around the carotid artery lumen. We use the gradient image because it accentuates the artery walls due to the sudden change in gray-level between the wall and the lumen. We choose the node in which its centroid has the smallest Euclidean distance compared to the centroid of the IM, found on step 3.2. Usually, the carotid artery wall is not entirely represented by a single max-tree node (Figure 27(b)), and the EM will work better if it enclosures all the entire lumen. Therefore, the final EM was composed of a circle of diameter equal 1.5 times the greatest distance between the pixels of the selected max-tree node and the manual seed. The diameter is not allowed to exceed 7.7 mm, the assumed maximum diameter for the CCA ((LIMBU *et al.*, 2006)).

By adjusting the EM diameter, we improve tie-zone watershed transform done on the next step, once a large EM can create leakages on the final result and a small EM, *ie*, with a diameter smaller than CCA lumen diameter, can make us lose information.

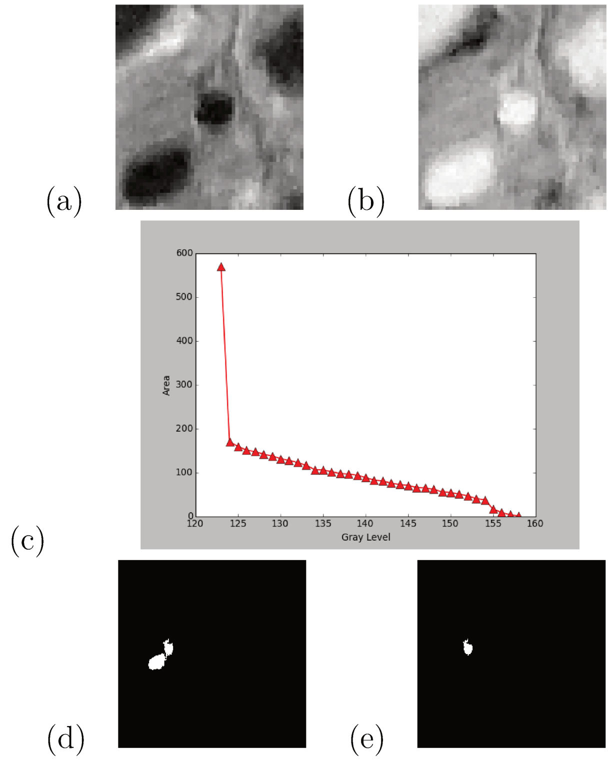

Figure 25 – (a) Original Image: CCA lumen can be seen as a dark structure (b) Negated Image: In this case, CCA lumen is a bright structure (c) Max-tree signature of negated image for structures smaller than 46.6 mm^2 (d) Image representing the node before the fall on signature in (c) (e) Image representing the node after the fall on signature in (c).

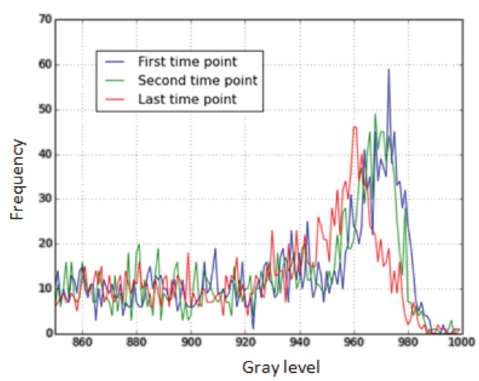

Figure 26 – Intensity histograms from the same slice at different time points are similar (Kolmogorov-Smirnov test found no significant differences between the three histograms, $p = 0.918$)

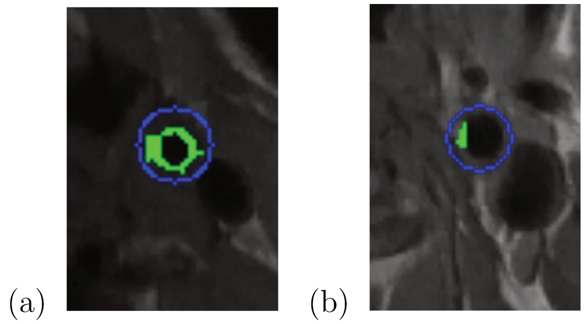

Figure 27 – Example of external markers. (a) In green, node representing the entire vessel wall (smallest Euclidean distance compared to the manually selected seed point). In blue, final external marker (b) In green, case where there is no node representing the entire vessel wall. In blue, final external marker

3.4 Tie-Zone Watershed Transform

The tie-zone watershed transform using the selected internal and external markers is applied to the gradient image.

3.5 Tie-Zone Assignment

As explained on 2, the tie-zone watershed returns regions that have the same cost value for both lumen and vessel wall. Those pixels, named here as tie-zone pixels, need to be correctly assigned to improve the method accuracy. The tie-zone pixels are then assigned using RF classifier. The classification is performed pixel-by-pixel. The features extracted for each tie-zone pixel are LBP, HOG, tie-zone labels histogram, gray level of the pixel and mean gray level of 8-neighbors around the pixel. The histograms (tie-zone histogram and HOG) are computed on a three by three window centered in the tie-zone pixel (Figure 28). All features are computed in the original image.

3.6 Chapter Conclusions

In this chapter we presented the segmentation methodology dividing it into five steps: Centroid selection, internal marker selection, external marker selection, tie-zone watershed transform and tie-zone thinning. An example of the final result can be seen on (Figure 29)

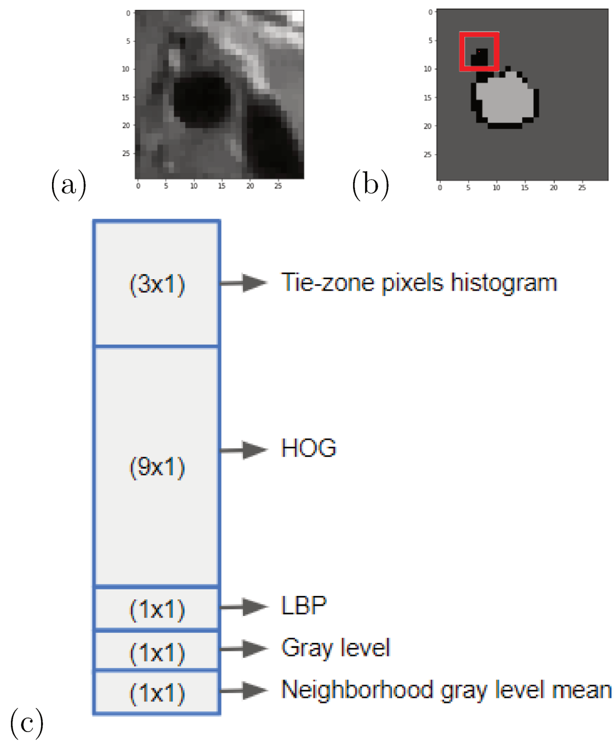

Figure 28 – Overview of our tie-zone classification methodology for carotid artery segmentation. (a) Original Image. (b) Tie-zone watershed transform. White zones are always labeled as lumen, gray zones always labeled as background. The black zone represent the tie-zone pixels. (c) Feature extraction of the highlighted pixel on image (b). Each feature vector has 15 components and there is one feature vector for each tie-zone pixel.

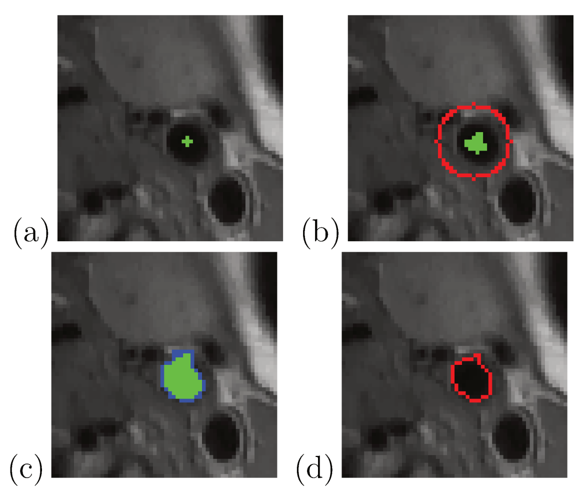

Figure 29 – Methodology overview for segmenting a left common carotid artery. (a) Automatic selected seed (represented here as green cross). (b) Internal (green) and external (red) markers. (c) Tie-zone watershed result (tie-zones in blue). (d) Segmentation result after tie-zone classification (red).

4 Results and Discussion

4.1 Introduction

In this chapter we will present and discuss results obtained from the application of the methodology explained on the previous chapter. The results demonstrate the automatic segmentation of the CCA lumen compared with manual segmentation of three different experts and a final consensus. Also we will present a best case scenario where we can see the best result we could achieve by using tie-zone methodology and we will also analyze the effects of removing the tie-zone step of the algorithm. Finally, we will do an feature analysis of tie-zone classification. For all experiments of this work, we used a dataset composed by 10 sequencies of healthy subjects, each one with 16 temporal bins. More information obout the dataset will be given below.

4.2 Centroid Selection

4.2.1 Dataset

In order to increase the classification robustness for centroid selection, we performed data augmentation, created a new dataset with rotated, shifted and re-scaled images derived from the cine FSE images (Figure 30)

Finally, our training and validation set was composed by 105 sequences of 16 temporal bins, including the augmented data. For testing, we had 25 sequences of images composed only by real images, unknown by the classifier. It is important to emphasize that despite the input of the automatic centroid selection algorithm is the sequence of 16 temporal bins, the input of the classifier is not an image, but the extracted feature matrix, explained on chapter 3.

4.2.2 Classification

- Training and validation

  After extracting all features from the training images, we ended up with 8107 candidate pairs, being only 126 of those true carotid pairs. In order to avoid underfitting due unbalanced dataset, the candidate pairs were shuffled and some of false examples were

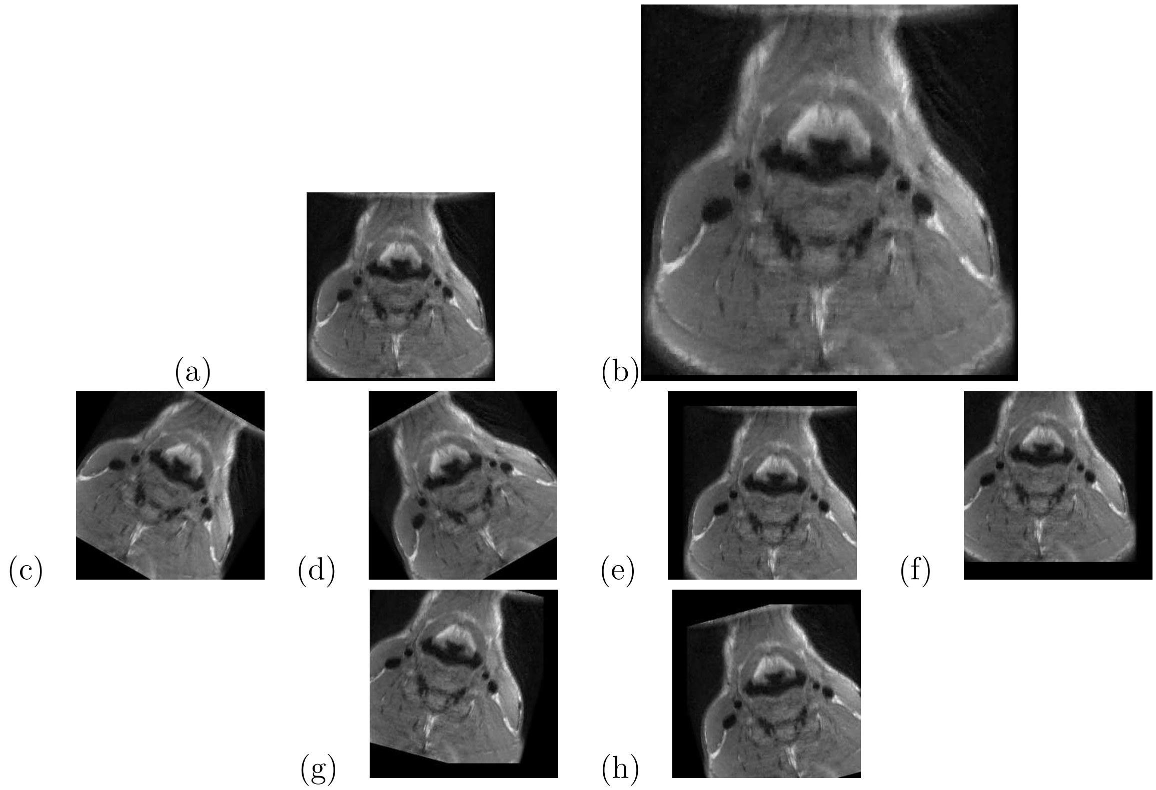

Figure 30 – New dataset created to simulate patient movement during acquisition (a) Original image (b) Re-scaled Image (c) Rotated 30º left (d) Rotated 30º right (e) shifted 20 pixels right and down (f) shifted 20 pixels left and up (g) Rotated 15º left and shifted (h) Rotated 15º right and shifted

ignored. Finally, we had 1000 pairs, 874 being false examples and 126 of true examples. This dataset was divided into 70% for training and 30% for validation.

In order to decide the best classifier to be used also ran Logistic Regression (LogR) and Suport Vector Machine (SVM) classifiers on training and validation dataset, however, as we can see on table 3, RF presented the best results.

Table 3 – Comparison between classifiers (RF, LogR and SVM). Here we can see Precision and Recall of the positive class, that means, the class that represents the true candidate pairs. As we can see, RF had the best results.

Classifier	**Training**		**Validation**	
	Precision	**Recall**	**Precision**	**Recall**
RF	**1**	**1**	**0.96**	**0.90**
LogR	0.82	0.81	0.80	0.83
SVM	0.92	0.99	0.89	0.86

As we explained before, despite the input of the algorithm is an image, RF receives a

(a) (b) (c)

Figure 31 – Examples of centroid automatic selection

feature matrix as input. So, in some cases, it returned more than one pair of candidates as centroid or, in other cases, none. In order to avoid these issues, instead of using a binary classifier, we analyze the probability returned by the RF. The pair with higher probability is assigned as centroids. Doing so, we increase our final accuracy.

- Testing

  Despite our classifier encountered some mistaken samples, as we can see on the confusion matrix (Table 4), when we have the final result given by the candidate pair with highest probability, we achieve 100% of accuracy on our test set. Some examples can be seen on Figure 31.

Table 4 – Confusion Matrix for test set. As we can see, there are 3 false negatives and 18 false positives. Using the classifier probability, we have 100% of accuracy on test set.

	0	**1**
0	2545	18
1	3	22

4.3 Segmentation

4.3.1 Dataset

Our dataset is composed by a total of 5 different acquisitions of 10 healthy subjects, totalizing 50 sequences of 16 temporal bins with a resolution of 0.6 x 0.6 x 2 mm3. However, one subject was discarded due to lack of manual segmentation (Figure 32).

4.3.2 Tie Zone Assignment Classifier

In order to assess RF as the best classifier to the project, we made some tests using LogR and SVM classifiers. As we can see on Table 5, the results are very similar, specially between RF and SVM, that presented the same accuracy and F1-Score. Between those two, RF was chosen due the processing time, that is smaller than SVM.

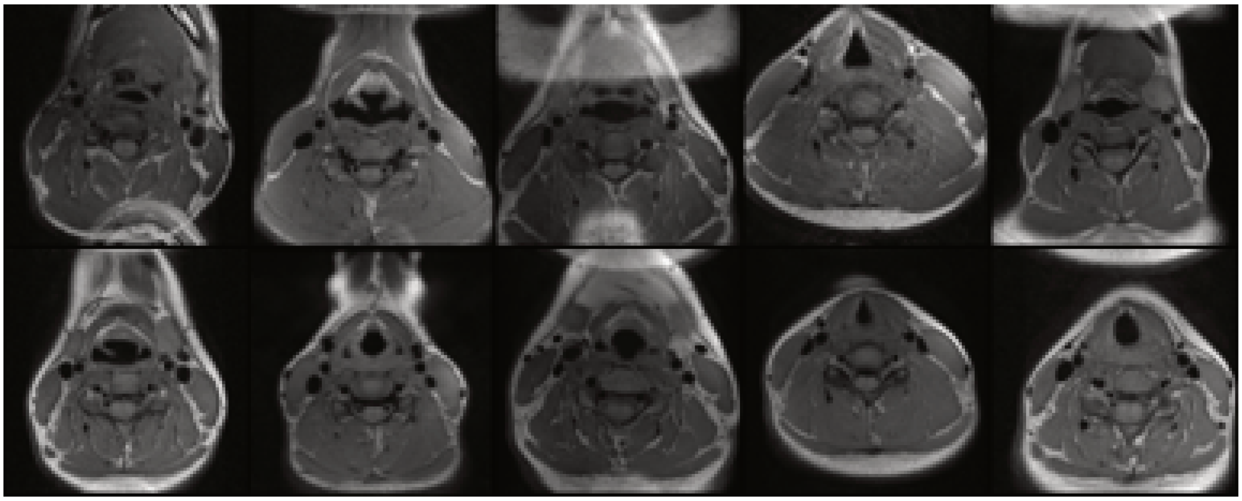

Figure 32 – 2D slice of each healthy subject

.

Table 5 – Comparison between classifiers (RF, LogR and SVM) for Tie-Zone assignment. Here we can see Precision, Recall, F1-Score and Accuracy for test results.

Classifier	**Precision**	**Recall**	**F1-Score**	**Accuracy**
RF	0.81	0.80	0.80	0.81
LogR	0.81	0.80	0.79	0.80
SVM	0.80	0.81	0.80	0.81

4.3.3 Ground Truth

We used the manual segmentation of three different specialists and their segmentation voting consensus to assess our results (Figure 33). The manual segmentation was done on Osirix plataform only for left CCA.

4.3.4 Final Results

For tie-zone classification, RF classifier could not have access to all subjects during training and validation. Therefore, to train and validate the RF, we used k-fold cross validation, dividing the dataset into 3 folds composed of 15 images from 3 different subjects each (34). As final results, we have the cross validation average. This was done during all the subsequent results shown on the next sections.

The final results can be seen on Table 6, where we compare the automatic segmentation with the voting consensus and with each expert segmentation individually. Figure [35] shows some of the best and some of the worst cases of segmentation results.

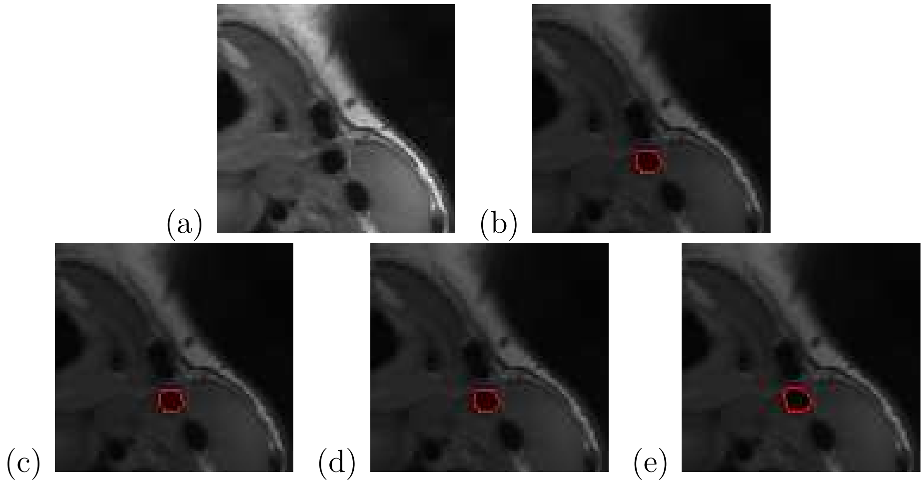

Figure 33 – Ground Truth Example (a) Original Image (b) Voting Consensus (c) Specialist 1 (d) Specialist 2 (d) Specialist 3

Table 6 – Dice coefficient, sensitivity and false positive rate (FPR) metrics. Averages (mean ± standard deviation shown) across all 3 folds are reported comparing automatic segmentation (AS) against the manual segmentation majority voting consensus (VC) and experts (Exp).

	Sensitivity	**Dice**	**FPR**
AS x VC	0.909 ± 0.011	0.926 ± 0.005	0.056 ± 0.003
AS x Exp1	0.923 ± 0.005	0.906 ± 0.011	0.057 ± 0.003
AS x Exp2	0.896 ± 0.01	0.905 ± 0.009	0.084 ± 0.007
AS x Exp3	0.90 ± 0.013	0.914 ± 0.004	0.071 ± 0.009
Exp1 x Exp2	0.921 ± 0.005	0.918 ± 0.008	0.075 ± 0.005
Exp1 x Exp3	0.941 ± 0.004	0.941 ± 0.006	0.057 ± 0.009
Exp2 x Exp3	0.908 ± 0.011	0.908 ± 0.005	0.057 ± 0.009

Analyzing table 6, we can see that our method can be comparable with experts segmentation. In fact, when we compare the automatic segmentation *versus* expert 3, we notice a bigger dice than comparing two experts segmentation (Expert 2 and Expert 3).

4.3.5 Processing Time

On Figure 36 we can see the amount of time that each step of the process takes. Although TZ assignment seems to be the least efficient algorithm, taking longer time to process, it is important to emphasize that feature selection algorithm (inserted into TZ assignment) is all written in Python programming language, while centroid selection, internal and external markers are based on a efficient Max-Tree library, written in programming language C.

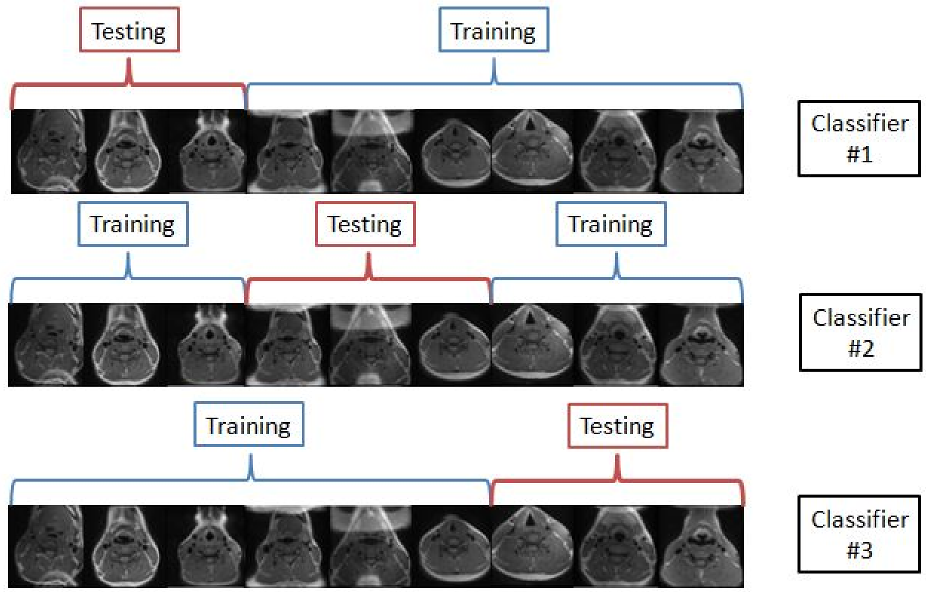

Figure 34 – Cross Validation scheme. Subjects were randomly partitioned into 3 folds containing 15 images from 3 different subjects (5 acquisitions per subject).

4.4 Algorithm analysis - Tie-Zone assignment

4.4.1 Watershed from markers x Tie-zone assignment

The methodology proposed is composed by many steps, which increases its complexity and processing time as shown on the previous topic. One of the less efficient steps is TZ algorithm, which is responsible for a increase of 1.3s, which is almost 47% of the processing time. In order to analyze the importance of this step, we generated new results, removing the TZ assignment of the methodology and leaving the segmentation only with the watershed with markers, explained on Chapter 2. Although TZ increase the final processing time, it also increases 2.3% in accuracy, leading to approximately 24% of error reduction. As this is an introductory study, an optimization work can be done on the code aiming to reduce the processing time, once we had an important accuracy increase and error reduction resulted by the addiction of TZ. The comparison between both cases can be seen on Table 8

4.4.2 Feature Analysis

Using RF classifier we run a feature analysis, where we can see which features are more important to classify the tie-zone pixels. This can be seen on table 7.

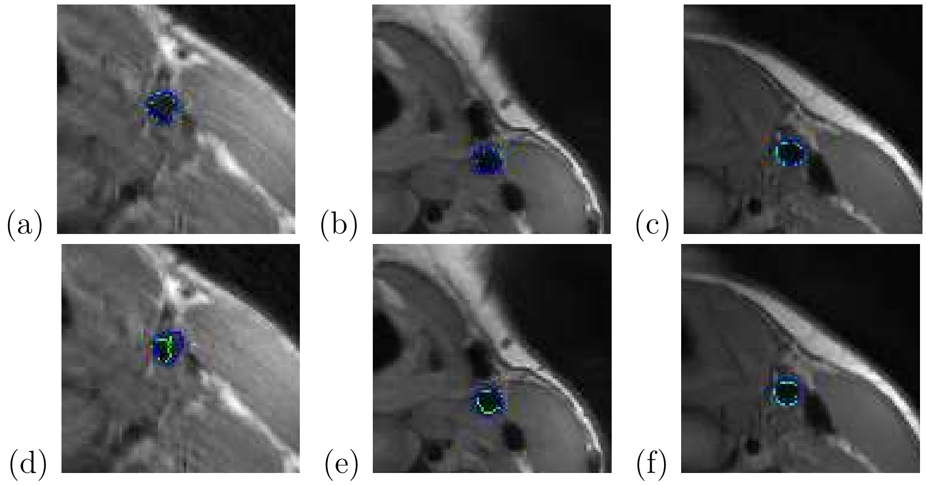

Figure 35 – Examples of one aquisition, taken from three different patients. Final automatic segmentation result in green and VC in blue. First line: Best results. Second line: worst results. (D = Dice, S = Sensitivity) (a) S = 0.94 |D = 0.95 |FPR = 0.05 (b) S = 0.98 |D = 0.97 |FPR = 0.05 (c)S = 0.931 |D = 0.922 |FPR = 0.089 (d) S = 0.47 |D = 0.63 |FPR = 0.01 (e) 0.83 |D = 0.90 |FPR = 0.02 (f) S = 0.89 |D = 0.89 |FPR = 0.12

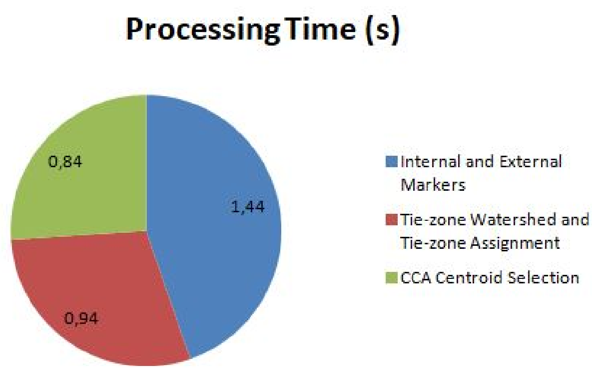

Figure 36 – Sequence of 16 temporal bins of the same slice during the cardiac cycle (zoom in around a CCA) collected with Cine FSE technique.

Table 7 – Feature importance for RF classifier, in order of importance (TZ Hist: Tie Zone Histogram; Glv Mean: Gray level of 8-neighbor window; Glv: gray level of pixel

Glv	**TZ Hist [2]**	**Glv Mean**	**TZ Hist [1]**	**HOG[1]**	**HOG[2]**	**LBP**	**HOG[0]**
0.21	0.21	0.20	0.14	0.05	0.04	0.03	0.03
HOG[3]	**HOG[4]**	**HOG[5]**	**TZ Hist [0]**	**HOG[6]**	**HOG [7]**	**HOG [8]**	
0.03	0.03	0.03	0.02	0	0	0	

As we can see, tie zone histogram and gray level information are the features with bigger importance.

4.4.3 Best Case Scenario

In order to analyze the Tie-Zone methodology, we created a best case scenario, in which we labeled all the TZ pixels according the voting consensus. The result of this experiment return the best result we could achieve by using the TZ. In other word, this is the result we would achieve by finding 100% of accuracy on RF classifier.

Table 8 shows us the final best case scenario results and compares them with the previous discussed results.

Table 8 – Comparison between Ti-zone Assignment results, Watershed with markers and the best case solution.

Method	TZ Assignment			Watershed from Markers			Best Case Scenario		
	Sensitivity	Dice	FPR	Sensitivity	Dice	FPR	Sensitivity	Dice	FPR
Method x VC	0.909 ± 0.011	0.926 ± 0.005	0.056 ± 0.003	0.859 ± 0.018	0.903 ± 0.003	0.043 ± 0.02	0.937 ± 0.008	0.96 ± 0.001	0.015 ± 0.008
Method x Exp1	0.923 ± 0.005	0.906 ± 0.011	0.057 ± 0.003	0.90 ± 0.003	0.856 ± 0.018	0.044 ± 0.018	0.947 ± 0.001	0.924 ± 0.008	0.027 ± 0.008
Method x Exp2	0.896 ± 0.01	0.905 ± 0.009	0.084 ± 0.007	0.856 ± 0.023	0.893 ± 0.002	0.061 ± 0.027	0.908 ± 0.014	0.923 ± 0.008	0.059 ± 0.018
Method x Exp3	0.90 ± 0.013	0.914 ± 0.004	0.071 ± 0.009	0.85 ± 0.011	0.891 ± 0.004	0.058 ± 0.022	0.915 ± 0.002	0.934 ± 0.004	0.043 ± 0.01

Figure 37 shows us the comparison between the three previous cases: Automatic segmentation, algorithm without tie-zone and best case scenario.

4.5 Chapter Conclusions

In this chapter we presented final results and discussions based on the developed methodology.

Based on the results and discussion presented on this chapter, we can conclude that the Tie-Zone assignment is the most complex part of the method, and besides it has shown to be better than watershed with markers, we can see there are improvements to be done on the Random Forest classifier, based on best case scenario and feature analyses.

Finally, we can conclude that the segmentation methodology based on tie-zone watershed and random forest classifier with internal and external markers found by a max-tree-based algorithm returned satisfactory results. If we analyze Table 6, we can notice that our final dice (against the vote consensus) is comparable with dice between the experts. In fact, only the combination Exp1 x Exp3 presented a higher score than the one presented by our method.

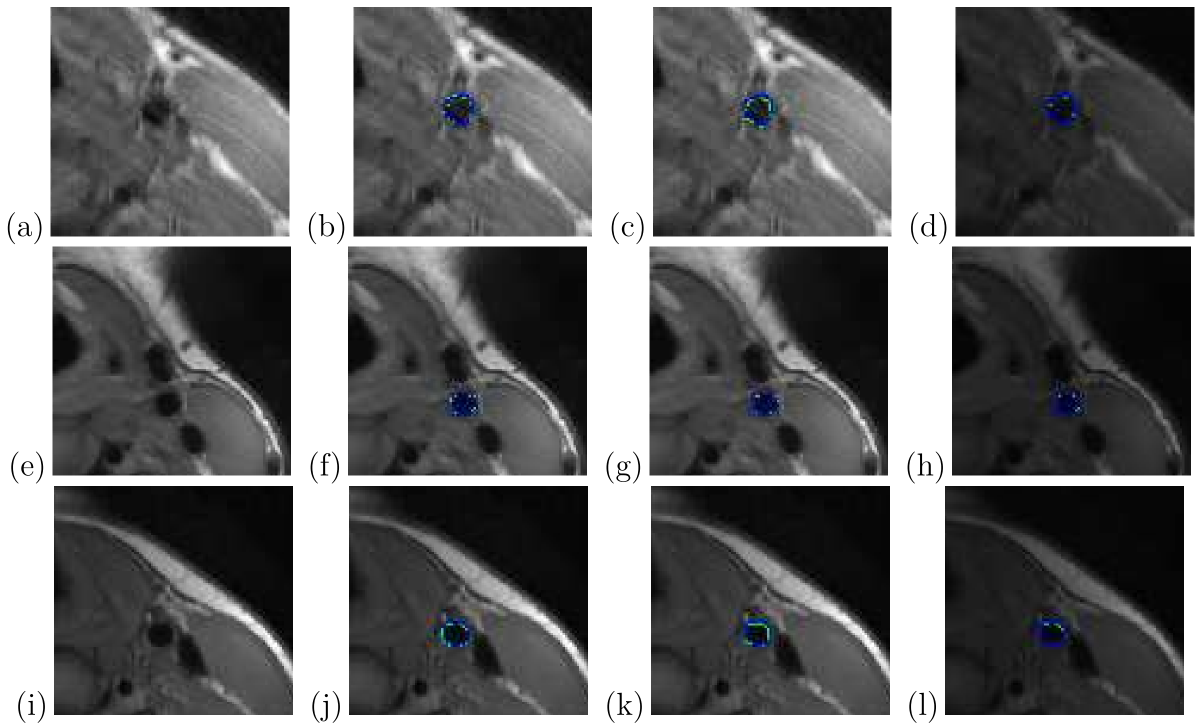

Figure 37 – We can see the final automatic segmentation result in green and the VC in blue. First column: Original Image; Second Column: Tie-Zone Assignment; Third Column: Watershed with markers; Fourth column: Best Case scenario.

5 Conclusions

5.1 Final Thoughts and Future Work

This work presented a new methodology proposal for CCA lumen segmentation. Despite there are some vessel segmentation methods described on the literature, we could not find any using Cine FSE images. We can not make a direct comparison between the results on the literature, once the dataset and the image nature are different. However we can see that our results are relatively close with the state of art. (UKWATTA *et al.*, 2013) reported a dice coefficient of 0.93 in statical 3T images. Our final dice was 0.92. Despite a lower result, we take in account the fact that our dataset is more challenger once Cine FSE images have lower resolution. Besides, analyzing Table 6, we can conclude that our automatic method is comparable with human manual segmentation. Also, currently in the literature, the segmentation methods available are semi-automatic, with human interaction at some level. We developed a fully automatic method, including the centroid selection. We could not find any public dataset of the images presented on papers in order to do an adequate comparison.

We can notice that there is still room for improvements on the method, specially on tie-zone assignment algorithm. When we analyze the best case scenario, we can notice that the classifier still loses information. Analyzing those results and feature analysis (Table 7) together, we can conclude that the features selection can be improved, either removing some of them (for instance, those that returned zero importance) or adding some more relevant features for the problem.

Between the difficulties found in the project, we can cite the low resolution of cine FSE images and high presence of artifacts (Figure 32), which increased the complexity of the methods. Also, we can cite the low quantity of images available for this study. At first, we only had two subjects to work with and no ground truth available for them, reason why those two images were not part of the final dataset for the method development. Finally, the second dataset available (used on the project) had only the manual segmentation of the left CCA, which reduced our dataset. In order to improve the method, it is necessary a greater amount of images. Despite we found good results, a bigger dataset would bring us more robust results.

For future work, it would be interesting to expand the method beyond CCA for segmenting carotid bifurcation and atherosclerotic plaque. With plaque segmentation we can also create a component study and analysis of the patient vulnerability. Besides, this work is part of a bigger project which aims to identify patients with atherosclerosis disease yet in earlier stages. For the segmentation method implemented here, we did not use dynamic information of the images, however, as future work, we can do a study of distensibility curves. This study is based on the hypothesis that the more rigid the vessel wall, bigger the chance of the patient to have atherosclerotic disease. Therefore, cine FSE images are necessary not only for minimizing movement artifacts, as said before, but for allowing the visualization of expansion and contraction of carotid during cardiac cycle, allowing analysis of the elasticity.

To a better analysis of the curves, it would be necessary to have the sequence referent to other positions of carotid artery. However, another limitation of our dataset was to present only one sequence of 16 temporal bins. While cine FSE images usually presents 8 sequences of N temporal bins each, being able to show bifurcation, our dataset only contained CCA images.

5.2 Publications

The following articles were published as a result of this research.

5.2.1 Conference Articles

- **Rodrigues, L**; Souza, R; Rittner, L; Frayne, R; Lotufo, R. Common Carotid Artery Lumen Segmentation from Cardiac Cycle-Resolved Cine Fast Spin Echo Magnetic Resonance Imaging In: 2017 30th SIBGRAPI Conference on Graphics, Patterns and Images (SIBGRAPI), 2017, Niteroi. 2017 30th SIBGRAPI Conference on Graphics, Patterns and Images (SIBGRAPI). IEEE, 2017. p.442 -

- **Rodrigues, L**; Souza, R; Rittner, L; Frayne, R; Lotufo, R. Common Carotid Artery Lumen Automatic Segmentation from Cine Fast Spin Echo Magnetic Resonance Imaging, SIPAIM – MICCAI Biomedical Workshop, Granada, 2018

5.2.2 Abstracts

- **Rodrigues, L**; Souza, R; Rittner, L; Frayne, R; Lotufo, R. Common Carotid Artery Lumen Segmentation from Cardiac Cycle-resolved Cine Fast Spin Echo Magnetic Resonance Imaging In: Society for Magnetic Resonance Angiography Annual COnference, 2017, Stellenbosch.

- **Rodrigues, L**; Souza, R; Rittner, L; Frayne, R; Lotufo. Semi-automatic Common Carotid Lumen Segmentation on Dynamic MR Images In: Canadian Stroke Congress, 2017, Calgary.
- **Rodrigues, L**; Souza, R; Rittner, L; Frayne, R; Lotufo. Common Carotid Lumen Segmentation using Cine Fast Spin Echo Magnetic Resonance In: 4rd Brainn Congress, 2017, Campinas.

Bibliography

AHONEN A. HADID, M. P. T. Face description with local binary patterns: Application to face recognition. *IEEE Transactions on Patterns Analysis and Machine Intelligence*, v. 28, p. 2037–41, 2006. Citado na página 31.

ARIAS-LORZA, A. M.; PETERSEN, J.; ENGELEN, A. van; SELWANESS, M.; LUGT, A. van der; NIESSEN, W. J.; BRUIJNE, M. de. Carotid artery wall segmentation in multispectral mri by coupled optimal surface graph cuts. *IEEE Transactions on Medical Imaging*, v. 35, n. 3, p. 901–911, 2016. ISSN 0278-0062. Citado na página 17.

AUDIGIER, R.; LOTUFO, R. A.; COUPRIE, M. The tie-zone watershed: definition, algorithm and applications. In: *IEEE International Conference on Image Processing 2005*. [S.l.: s.n.], 2005. v. 2, p. II–654–7. Citado na página 26.

BOESEN, M.; NETO, L. M.; PULWICKI, A.; YERLY, J.; LEBEL, M.; R. Fast spin echo imaging of carotid artery dynamics. *Magnetic Resonance in Medicine*, v. 74, n. 4, p. 1103–1109, 2015. Citado 2 vezes nas páginas 15 and 20.

BREIMAN, L. Random forests. *Mach. Learn.*, v. 45, n. 1, p. 5–32, 2001. Citado 2 vezes nas páginas 19 and 29.

CRIMINISI, J. S. A.; KONUKOGLU, E. Decision forests: A unified framework for classification, regression, density estimation, manifold learning and semi-supervised learning. *Foundations and Trends® in Computer Graphics and Visiong*, v. 7, p. 81–227, 2012. Citado 2 vezes nas páginas 27 and 28.

DALAL, N.; TRIGGS, B. Histograms of oriented gradients for human detection. *IEEE CVPR*, v. 1, p. 886–893, 2005. Citado na página 31.

DOUGHERTY, E. A.; LOTUFO, R. Hands-on morphological image processing. *SPIE Tutorial Texts in Optical Engineering*, 2003. Citado 2 vezes nas páginas and 25.

JONES, R. Connected filtering and segmentation using component trees. *Computer Vision and Image Understanding*, Elsevier Science Inc., New York, NY, USA, v. 75, n. 3, p. 215–228, 1999. Citado 2 vezes nas páginas 19 and 22.

LESAGE, D.; ANGELINI, E.; BLOCH, I.; FUNKA-LEA, G. A review of 3d vessel lumen segmentation techniques: Models, features and extraction schemes. *Medical Image Analysis*, v. 13, n. 6, p. 819 – 845, 2009. ISSN 1361-8415. Includes Special Section on Computational Biomechanics for Medicine. Citado na página 17.

LIMBU, Y.; GURUNG, G.; MALLA, R.; RAJBHANDARI, R.; REGMI, S. Assessment of carotid artery dimensions by ultrasound in non-smoker healthy adults of both sexes. *Nepal Med Coll*, v. 8, p. 200–3, 2006. Citado 3 vezes nas páginas 36, 38, and 39.

LOPEZ V.NARANJO, J. A. E. V. M. A. S. L. F. Aorta segmentation using the watershed algorithm for an augmented reality in laparoscopic durgery. In: *2011 IEEE International Conference on Image Processing*. [S.l.: s.n.], 2011. p. 2649–2652. ISSN 4577-1303. Citado na página 18.

LOTUFO, R.; FALCãO, A.; ZAMPIROLLI, F. Ift-watershed from gray-scale marker. *Computer Graphics and Image Processing*, p. 146–152, 2002. Citado na página 19.

LUSTIG, M.; DONOHO, D.; PAULY, J. Sparse mri: The application of compressed sensing for rapid mr imaging. *Magnetic Resonance in Medicine*, Wiley Subscription Services, Inc., A Wiley Company, v. 58, n. 6, p. 1182–1195, 2007. Citado na página 20.

MENDES, J.; PARKER, D.; J.HULET; TREIMAN, G.; KIM, S. Cine turbo spin echo imaging. *Magnetic Resonance in Medicine*, Wiley Subscription Services, Inc., A Wiley Company, v. 66, n. 5, p. 1286–1292, 2011. ISSN 1522-2594. Citado 2 vezes nas páginas 15 and 20.

NAGHAVI, M. From Vulnerable Plaque to Vulnerable Patient: A Call for New Definitions and Risk Assessment Strategies: Part I. *Circulation*, v. 108, n. 14, p. 1664–1672, out. 2003. Citado 2 vezes nas páginas and 16.

SAAM, T.; HATSUKAMI, T.; TAKAYA, N.; CHU, B.; UNDERHILL, H.; KERWIN, W.; J.CAI; FERGUSON, M.; YUAN, C. The vulnerable, or high-risk, atherosclerotic plaque: Noninvasive mr imaging for characterization and assessment. *Radiology*, v. 244, n. 1, p. 64–77, 2007. Citado 2 vezes nas páginas 15 and 20.

SAKELLARIOS, A. I.; STEFANOU, K.; SIOGKAS, P.; TSAKANIKAS, V.; BOURANTAS, C.; ATHANASIOU, L.; EXARCHOS, T.; FOTIOU, E.; NAKA, K.; PAPAFAKLIS, M.; PATTERSON, A.; YOUNG, V.; GILLARD, J.; MICHALIS, L.; FOTIADIS, D. Novel methodology for 3d reconstruction of carotid arteries and plaque characterization based upon magnetic resonance imaging carotid angiography data. *Magnetic Resonance Imaging*, v. 30, p. 1068–82, 2012. Citado na página 18.

SALEMBIER, P.; OLIVERAS, A.; GARRIDO, L. Antiextensive connected operators for image and sequence processing. *IEEE Transactions on Image Processing*, v. 7, n. 4, p. 555–570, 1998. Citado 2 vezes nas páginas 19 and 23.

SOUZA, R.; RITTNER, L.; MACHADO, R.; LOTUFO, R. Maximal max-tree simplification. In: *Pattern Recognition (ICPR), 2014 22nd International Conference on*. [S.l.: s.n.], 2014. p. 3132–3137. ISSN 1051-4651. Citado 2 vezes nas páginas 21 and 23.

UKWATTA, E.; YUAN, J.; RAJCHL, M.; QIU, W.; TESSIER, D.; FENSTER, A. 3-d carotid multi-region mri segmentation by globally optimal evolution of coupled surfaces. *IEEE Transactions on Medical Imaging*, v. 32, p. 770–785, 2013. Citado 2 vezes nas páginas 17 and 52.

YUAN, C.; MITSUMORI, L.; BEACH, K.; MARAVILLA, K. Carotid atherosclerotic plaque: Noninvasive mr characterization and identification of vulnerable lesions. *Radiology*, v. 221, n. 2, p. 285–299, 2001. Citado 2 vezes nas páginas 15 and 20.